Chapter 5
Semiconductor Waveguides

Abstract Semiconductor optical waveguides are a very important part of modern integrated optoelectronic systems, especially for electrically active devices. Applications range from semiconductor lasers, optical filters, switches, modulators, isolators, and photodetectors. Semiconductor waveguides have many advantages especially for use in slow light applications. They offer a significant enhancement of interaction length that, to first order, scales with the possible delay. With a tight confinement of the optical mode, the required optical power can be drastically reduced while the mode overlap with the active material is strongly enhanced. The use of semiconductor material is of particular interest since it offers compactness and enables for monolithic integration into optoelectronic devices using well established processing techniques. Furthermore, semiconductors are attractive since the operating wavelength, to a large extend, can be designed while performing with bandwidths in the GHz regime that is well suited for communication signals. Based on III–V, II–VI, or IV–VI group elements, two semiconductors with different refractive indices are generally synthesized for fabrication of optical waveguides. They must have different band gaps but same lattice constant. An attractive feature of the binary compounds is that they can be combined or alloyed to form ternary or quaternary compounds, or mixed crystals, for varying the band gap continuously and monotonically together with the variation of band structure, electronic, and optical properties. The formation of ternary and quaternary compounds of varying band gaps also enables the formation of heterojunctions, which have become essential for the design of high performance electronic and optoelectronic devices. This chapter will give a brief review about fundamental theory, semiconductor materials, and fabrication technologies of various semiconductor waveguides.

X.C. Tong, *Advanced Materials for Integrated Optical Waveguides*, Springer Series in Advanced Microelectronics 46, DOI 10.1007/978-3-319-01550-7_5,
© Springer International Publishing Switzerland 2014

5.1 Fundamental Theory

5.1.1 Crystal Structure

Atoms in solid-state materials are located at energetically most favorable sites. The locations depend on the characteristics of the atoms, such as their size and their electric structure. Generally, the ordering of the atoms can be monocrystalline, polycrystalline or amorphous. For example, III–V compound semiconductor materials are made by epitaxy with monocrystalline structure.

When materials crystallize, the atoms are arranged into a crystal lattice. The crystal lattice represents a set of points in space which form a periodic structure. The smallest repetitive structure in any crystal lattice is called the primitive unit cell. The whole crystal can be formed by repeating primitive unit cells. Primitive vectors are linearly independent and connect the lattice points of crystal lattice. Primitive vectors can be chosen by numerous ways and, therefore, primitive vectors are not unique. Primitive vectors have a useful property that all the lattice points $\mathbf{R}$ can be derived from one lattice point $\mathbf{R}_0$ when some linear combination of primitive vectors is added to it (Jussila 2010):

$$\mathbf{R} = \mathbf{R}_0 + m_1\mathbf{a}_1 + m_2\mathbf{a}_2 + m_3\mathbf{a}_3 \tag{5.1}$$

where m_1, m_2 and m_3 are integers, and $\mathbf{a}_1$, $\mathbf{a}_2$ and $\mathbf{a}_3$ are the primitive vectors. As a result of this, the whole crystal can be formed by choosing all combinations of the integer m_1, m_2 and m_3.

To illustrate this type of crystal lattice, a conventional unit cell of a face centered cubic (FCC) lattice is shown in Fig. 5.1a. Atoms in FCC lattice are located at every corner and at the center of every face of a cube. The zincblende lattice, for instance, is composed of two separate FCC sublattices one of which is comprised of group III atoms and the other of group V atoms. The dimensions of the two FCC-lattices are equal but the origin of the other lattice is displaced from the other by a vector ($a/4$; $a/4$; $a/4$) along the body diagonal. Figure 5.1b illustrates the conventional unit cell of a zincblende crystal lattice; the binary III–V compound semiconductors InAs, InP, GaAs, and GaP all are zincblende crystal, but with different lattice constant (Vurgaftman et al. 2001).

The crystal structure of a solid restricts the movement of carriers. In a semiconductor material, the outer electrons of the atoms are delocalized over the entire crystal, with the periodicity of the crystal structure limiting their movement. For certain electron energy, the carrier is allowed to move in one direction, but its motion in a different direction is restricted as a result of destructive interaction from the atomic lattice. This dependence of the electron energy on the momentum of the carrier results in a structure of energy bands where the carrier can exist (Hoogland 2013).

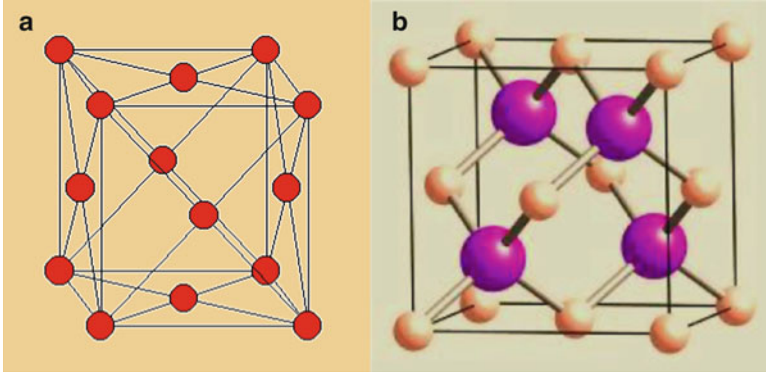

Fig. 5.1 Illustration of some crystal structures: (**a**) conventional unit cell of FCC lattice; (**b**) conventional unit cell of the zincblende lattice

5.1.2 Energy Band Structure

The energy band structure is used to explain the electronic structure of the material, which is derived from quantum mechanics. The foundation of quantum mechanics is the Schrödinger equation, represented in time independent form as (Jussila 2010),

$$\left(-\frac{h^2}{2m}\nabla^2 + V(\mathbf{r})\right)\psi(\mathbf{r}) = E\psi(\mathbf{r}) \tag{5.2}$$

where ∇ is the gradient, h is the Planck's constant, and m is the mass of the particle. $V(\mathbf{r})$ denotes the potential energy experienced by the particle. Typically in solids, potential energy is comprised of interactions between the particle and all the atoms in solids. In semiconductor crystals, the potential energy $V(\mathbf{r})$ is periodic and expressed as (Jussila 2010)

$$V(\mathbf{r}) = V(\mathbf{r} + \mathbf{a}) \tag{5.3}$$

where $\mathbf{a}$ is the primitive vector of the material. Periodicity of the atoms makes the energy states of crystals periodic in E–$\mathbf{k}$ space, where $\mathbf{k}$ is the electron wave vector. In addition, the semiconductor crystals have some energy states which are forbidden for every $\mathbf{k}$-vector. The relation between the electron wave vector $\mathbf{k}$ and the energy E is called the dispersion relation, which allowed energy states in E–$\mathbf{k}$ space form continuous energy bands. The two most important energy bands in semiconductors are the valence band and the conduction band. The valence band is defined as the highest occupied energy band, and the conduction band as the lowest empty energy band at the temperature of 0 K. Band gap of the material is

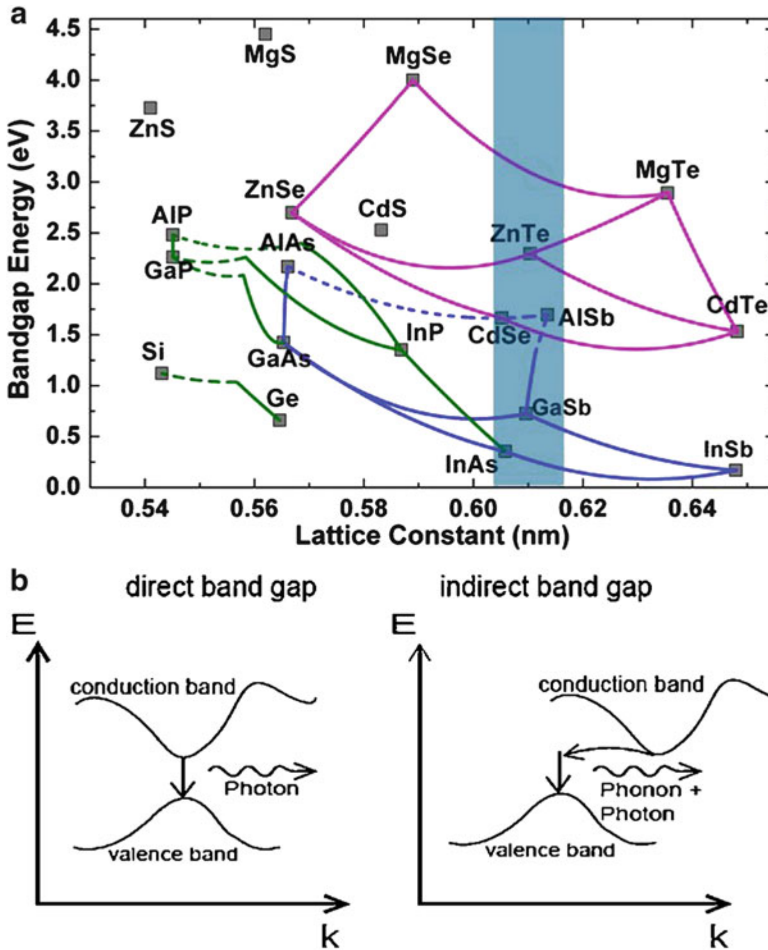

Fig. 5.2 Illustration of energy band structures: (**a**) band gap energy of III–V and II–VI semiconductors; (**b**) energy band structures and photon generation in direct and indirect band gap semiconductors

defined as the energy difference between the conduction band minimum and the valence band maximum. Figure 5.2a presents the band gap energy of III–V and II–VI compound semiconductors. All optical processes occurring in different materials follow the conservation laws of energy and momentum, and can be described with E–$\mathbf{k}$ diagrams. Semiconductors distinguish themselves from other materials by having an energy gap between the highest occupied energy band (the valence band) and the lowest unoccupied energy band (the conduction band). The band gap of a semiconductor is measured between the top of the valence band and the bottom of the conduction band and is called direct if these extrema coincide in momentum (e.g., GaAs) and is called indirect if they do not (Si), as shown in Fig. 5.2b. In direct band

gap materials, the conduction band minimum value is located at the same **k**-vector value as the valence band maximum value. The operation of optoelectronic devices that emit or amplify light is based on the phenomenon of either luminescence or stimulated emission. In these phenomena, an electron is relaxed from the conduction band to the valence band, thus generating a photon whose energy equals to the difference of these energy states. In indirect band gap materials, these phenomena are inefficient because the energy transition between the conduction band and the valence band requires a change in momentum which usually occurs via an interaction with a phonon. Therefore, optical-emitting transitions are most likely to occur in direct band gap materials, which are more commonly used in optoelectronic devices (Jussila 2010).

In the real world, the semiconductor crystal is finite, which puts restrictions on the allowed wave vectors within the energy bands, resulting in a set of discrete states available in each band with a wave vector separation determined by the size of the semiconductor (Hoogland 2013).

5.1.3 III–V Compound Semiconductors

III–V compound semiconductors are composed of group III and group V atoms. Binary compounds include InP, InAs, GaAs, and GaN. A fraction of the lattice sites in a binary semiconductor is replaced by other elements to form ternary (e.g., InGaAs, AlGaN) or quaternary (e.g., InGaAsP, InAlGaAs) compounds. For example, $Al_xGa_{1-x}As$ is made by replacing a fraction x of Ga atoms by Al atoms. Band gap varies with x as $E_g(x) = 1.424 + 1.247x$, when $0 < x < 0.45$. Quaternary compound $In_{1-x}Ga_xAs_yP_{1-y}$ is useful in the wavelength range of 1.1–1.6 μm. For matching lattice constant to InP substrate, $x/y = 0.45$. Band gap varies with y as $E_g(y) = 1.35–0.72y + 0.12y^2$. III–V compound semiconductors provide the possibility to engineer the band gap and the lattice constant by changing the composition of the different elements. Figure 5.3 shows the relation between the crystal lattice constant, the band gap energy and corresponding emission wavelength of different III–V compound semiconductors (Jussila 2010).

III–V semiconductors can provide significant advantages over other materials such as $LiNO_3$ or glass for many optical applications, which may include (Deri and Kapon 1991): (a) the potential for monolithic integration with other optoelectronic (e.g., lasers, detectors) and electronic (transistor) devices to enhance the functionality of transmitter or receiver circuits using additional guided-wave signal processing; (b) suitability for high-speed low-drive voltage modulators and switches, with further advances from multiple quantum-well (MQW) technology; and (c) the availability of sophisticated, controllable fabrication processes (e.g., epitaxial growth, selective etching) and simple methods for endfacet preparation (scribe-and-cleave versus cut and polish). For these reasons, interest in III–V semiconductor guided-wave devices continues to grow, particularly as single-mode optical waveguides have increasingly accepted for communications transmission applications.

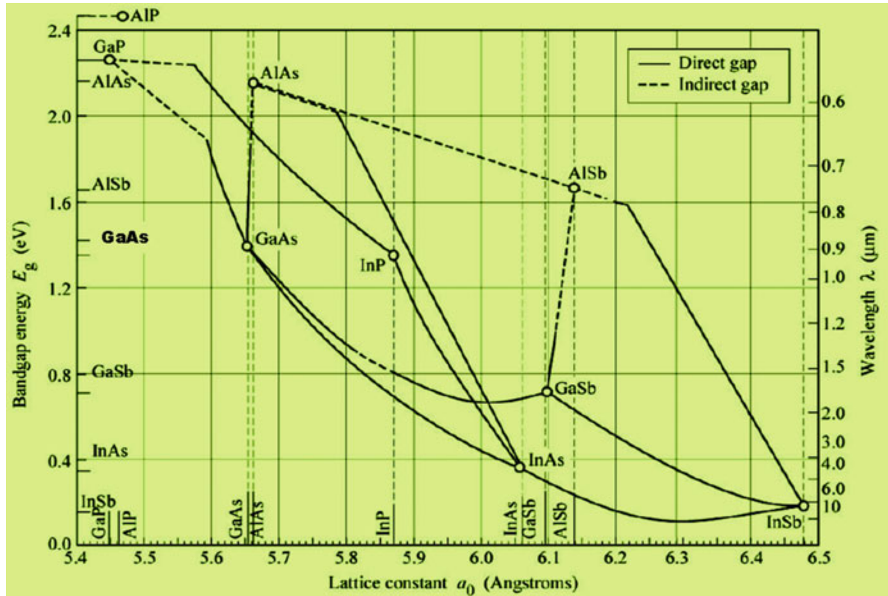

Fig. 5.3 Band gap and the lattice constant of different III–V compound semiconductor materials. The *lines* drawn in the image describe the lattice constant and the band gap of different ternary alloys. For instance, the band gap and the lattice constant of $In_{(1-x)}Ga_xAs$ is located on the *line* which is drawn between the binary compounds GaAs and InAs (Jussila 2010)

5.1.4 Quantum Structure

Quantum structures confine the charge carriers in one, two or three dimensions to such a small size that quantum mechanical effects are observed, as shown in Fig. 5.4. The structure which confines the charge carriers in one dimension is called a quantum well (QW). QWs can be fabricated by growing a layer of a small band gap material sandwiched between large band gap materials. Electrons in the small band gap material experience a potential energy well when moving along the growth direction. The structure which confines the charge carriers in two spatial dimensions is called quantum wire (QR). Quantum dots (QDs) confine the charge carriers in all three spatial dimensions. Fabrication of QDs can be performed by different methods, all of which result in a structure where a small band gap material is located inside a large band gap material (Jussila 2010).

As a practical matter, the states in a macro-size chunk of semiconductor are so closely spaced that the conduction and valence bands appear to be continua. The number of these states per unit volume in an energy band is described by the density of states. Because no available states exist within the band gap, the density of states is measured from the bottom of the conduction band and the top of the valence band from which it is, for a bulk semiconductor, a continuously increasing function with carrier energy (Fig. 5.4a). The magnitude is determined by the effective mass of the

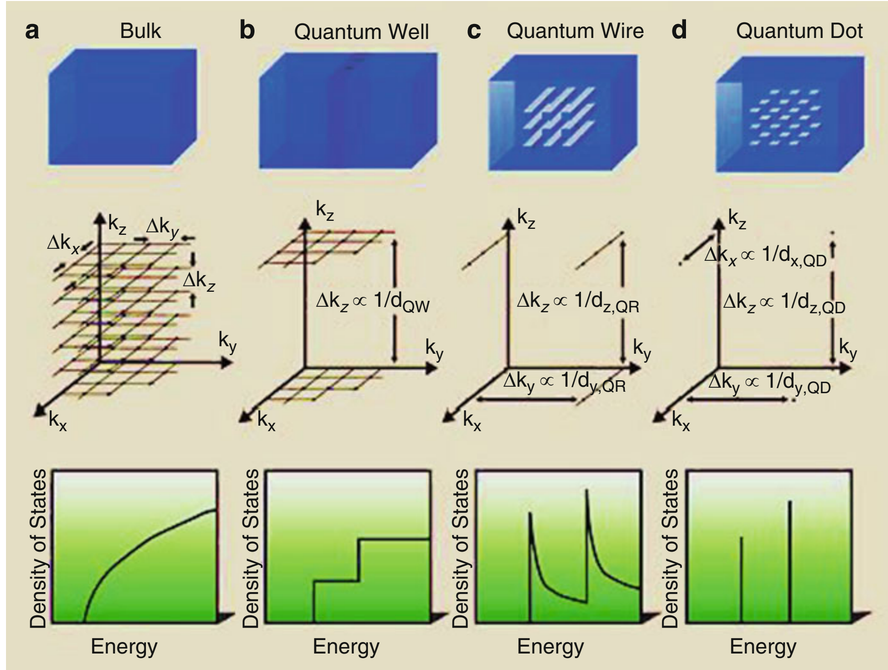

Fig. 5.4 Schematic illustrations of the active region (*top*), allowed states in momentum space (*middle*) and density of states (*bottom*) for confinement in no dimensions (i.e., bulk material) (**a**), in one dimension (i.e., a quantum well) (**b**), in two dimensions (i.e., a quantum wire) (**c**) and in three dimensions (i.e., a quantum dot) (**d**). *d* dimension(s) of quantum structure, *k* momentum, *QW* quantum well, *QR* quantum wire, *QD* quantum dot (Hoogland 2013)

carrier, which is a measure of the degree of curvature of the energy band around the extrema—the larger the curvature, the smaller the effective mass of the carrier; the larger the wave vector separation between states, the smaller the density of states. In semiconductors, electrons can be excited thermally to the conduction band, leaving holes in the valence band. Alternatively, electrons can be actively excited to the conduction band, for example, by absorbing a photon with energy larger than the semiconductor band gap. The excited carriers will thermalize very quickly to the bottom of the conduction band (electrons) and to the top of the valence band (holes) by losing energy through carrier–carrier and carrier–phonon scattering. The probability of finding an excited carrier at certain energy in a semiconductor at thermal equilibrium is described by temperature-dependent Fermi–Dirac statistics. The overall carrier distribution in a semiconductor thus is a function of both the density of states and of the temperature-dependent Fermi–Dirac distribution. In a bulk semiconductor, this distribution is widespread, with a small number of carriers right near the edge of the conduction and valence bands and with a peak that is situated above (below) the conduction (valence) band, whose position is temperature dependent. Because the emission spectrum depends

on the distribution and number of available transitions, a bulk semiconductor exhibits a temperature-sensitive emission spectrum, which is undesirable for stable lasing operation. Moreover, the temperature-dependent carrier distribution also makes the laser threshold temperature dependent. These unfavorable optical properties of bulk semiconductors can be overcome by confining carriers to dimensions approximating the de Broglie wavelength of the carriers. A quantum well can be formed by introducing a very thin layer of semiconductor whose band gap is less than that of the surrounding semiconductor (Fig. 5.4b). Charge carriers in this potential well can survive only when their energies correspond to wave functions that satisfy the boundary conditions for a standing wave. Because these wave functions depend on the quantum-well dimensions, the energies allowed in the well—and, hence, the effective band gap—are tunable by adjusting the well dimensions. When the size of the well becomes comparable to the de Broglie wavelength of the carrier, the energy separation between the resonances becomes large enough to form a discrete energy spectrum. The small width of the well results in the restriction of the carrier movement in the direction perpendicular to the well, causing the discrete energy spectrum. Because the width of the quantum well typically is several orders of magnitude smaller than the dimensions of the bulk semiconductor crystal, the wave vector separation between allowed states in the direction of the quantum well is greatly enlarged, compared with the bulk case (Fig. 5.4a, middle). However, carrier movement parallel to the well is unrestricted, just as in bulk material, thus yielding a dense distribution of states in plane parallel to the well (Fig. 5.4b, middle panel). Therefore, at each allowed quantum-confined level, the overall density of states is determined by the wave vectors parallel to the well, thus yielding a two-dimensional density of states: At each allowed energy level, a sharp increase of the density states occurs, as shown in the bottom panel of Fig. 5.4b. This shape results in a less temperature-sensitive carrier distribution than in bulk material, with the peak emission wavelength more stable around the quantum-confined transition energies. In addition, because of the increased number of carriers near the transition energy, the emitted light spectrum has a narrower bandwidth, the peak material gain is increased, and the transparency threshold is decreased. All these improvements in the optical properties arise from quantum confinement of carriers in only one dimension. When taking the degree of confinement to the maximum by creating a quantum dot, the carriers are restricted in their motion in all three dimensions, eliminating the possibility of bulk-like carrier motion. This leads to a truly discrete density of states exhibiting delta functions at the allowed energy states (Fig. 5.4d). Such shape is analogous to atomic energy levels, and therefore quantum dots also are known as artificial atoms. The number of charge carriers accumulated at the working transition is enlarged greatly at the expense of the higher energy parasitic states of the continuum. Therefore, 3D quantum confinement ensures not only temperature insensitivity of the emission wavelength but also the narrowest emission and gain bandwidths, as well as the lowest transparency threshold. An excited electron and hole can interact with each other through Coulomb attractions, creating a quasiparticle called an exciton. However, the binding energy required to create one is much smaller than the

thermal energy; therefore, excitons have a very low probability of existing in a bulk semiconductor at room temperature. In quantum-confined systems, and particularly in a quantum dot, the excited electron and hole are forced to exist very close to each other, causing large Coulomb interactions between them. In this case, the binding energy and oscillator strengths are increased, and the excitons can exist at room temperature. The degree of quantum confinement is determined by the interaction length over which the bond between an electron and a hole extends in an exciton, compared with the size of the quantum dot. In weak quantum confinement, the interaction length is shorter than the dimensions of the quantum dot, resulting in very closely spaced quantum-confined energy states. In this case, the quantum dot seems more bulk-like because the electron and hole can separate beyond the exciton interaction length, thus breaking up the exciton and making the transition energy independent of the quantum dot size. In the strong quantum confinement regime, the quantum dot size is smaller than the electron hole interaction length, resulting in widely spaced energy states. The quantum dot sizes can be so small that the energy spacing between the allowed states in the conduction and valence bands is large enough to cause a so-called phonon bottleneck. In most semiconductors, excited electrons can relax down to the bottom of the conduction band by losing energy through carrier–carrier and carrier–phonon interactions. However, a phonon bottleneck occurs when the spacing between energy states is much larger than these interaction energies—as is the case in strong quantum confinement. In this case, the probability for a carrier in a higher energetic state to lose its energy to a lower energetic state through these interactions becomes very low. As a result, electrons cannot relax to the bottom of the conduction band, and so quantum dots with strong quantum confinement should not be expected to emit light from the normal transition across the band gap. However, this phonon bottleneck has not been observed experimentally. This could be explained by the fact that fabricated quantum dots still are imperfect 3D quantum-confined systems (Hoogland 2013).

Quantum structures provide the possibility to engineer the energy band structure of the material. The dispersion relation of the conduction band is presented for bulk semiconductors and different quantum structures. The similar results are also valid for the valence band with the only difference then occurring in the effective mass of the electron, which is replaced by the effective mass of the hole in the valence band. The dispersion relation of the bulk material is assumed to be parabolic near the band edge (i.e., near the Γ-point, $\mathbf{k} = 0$). Hence (Jussila 2010),

$$E_{\text{bulk}}(\mathbf{k}) = E_{\text{g}} + \frac{h^2}{2m_{\text{e}}}\mathbf{k}^2 \tag{5.4}$$

where the E_{g} is the band gap of bulk material, and m_{e} the elective mass of electron. The zero of the energy is set at the valence band maximum. The dispersion relation of a QW with infinitely high barriers gives the following energy states (Jussila 2010):

$$E_{\text{QW}}(\mathbf{k}) = E_{\text{g}} + \frac{\pi^2 h^2 n^2}{2m_{\text{e}}L^2} + \frac{h^2}{2m_{\text{e}}}\mathbf{k}_{\|}^2 \tag{5.5}$$

where $\mathbf{k}_{||}$ is the wave vector component in the quantum-well plane, L the width of the quantum well, and n any integer. The solution is valid only near the energy band edge. The conduction band minimum ($n = 1$) for the QW is located at a different energy than for the bulk material, and the width of the quantum well affects the allowed energy states. Therefore, the energy band position of the QW structure can be engineered by varying the thickness of the QW.

For a spherical QD structure with infinitely high barriers the allowed energies are (Jussila 2010):

$$E_{\mathrm{QD}}(\mathbf{k}) = E_{\mathrm{g}} + \frac{h^2}{2m_{\mathrm{e}}}\left(\frac{k_{n,l}}{R}\right)^2 \tag{5.6}$$

where $k_{n,l}$ is the nth zero of lth Bessel function and R the radius of the quantum dot. The radius of the QD affects the energy states, so again the energy bands can be engineered by varying the size of the quantum structure. In addition to this, the energy states of QDs are completely discrete.

The height of the potential barrier was set to infinite to obtain previous results. In real semiconductor QW and QD systems this infinite potential well approximation is not true; and in fact, the height of the potential well also affects the allowed energy states of real quantum structures. However, the results obtained using this approximation provide insight into the nature of the energy states and are not far from the ones obtained by the more advanced numerical techniques.

Quantum structures provide attractive means to engineer the energy band structure of the material. In addition to this, quantum structures possess one extra advantage which is their density of state (DOS) function. DOS function explains how electrons can occupy the energy states of the structure. For instance, if the DOS function has a value of zero for some energy, then no electron can occupy that energy state. Figure 5.4 illustrates the DOS functions of different quantum structures. The DOS function in bulk materials is proportional to the square root of the energy. In quantum structures, the charge carriers are more strictly confined to specific energy states. QWs have a step-function-like DOS function and QDs have a delta-function-like DOS function. The delta-function-like DOS function is the main reason why QDs have been of great interest in recent years. This type of DOS function ensures that the charge carriers are strictly confined to the energy states described in (5.6). Therefore, QD structures enable the fabrication of components that, in principle, operate extremely efficiently. Semiconductor QDs can be fabricated by the following techniques (Jussila 2010).

Initially techniques used for the fabrication of QDs and quantum wires included lithography and etching steps. The etching step can result in degradation of the crystal structure of the material. Therefore alternative method called in situ growth of coherent (i.e., dislocation free) QDs has been used. This self-assembled technique is based on the Stranski–Krastanow growth mode of thin films. The term self-assembly refers to the behavior of the adsorbed atoms to form islands without any

external interactions. In this technique, the self-assembly emerges due to the crystal lattice mismatch between the two different materials; and as a result of this, QDs are then fabricated from these islands. As explained in the previous section, QDs emit luminescence at discrete energies because of their DOS function. However, the luminescence spectrum in real QD systems has not fully realized this promise and QD structures can have relatively broad luminescence spectra compared to QWs. This broadening originates from the fabrication processes of the QDs. For instance, the broadening in self-assembled QDs comes from the size distribution of the islands fabricated by the coherent Stranski–Krastanow growth mode. In practice, the growth conditions in the self-assembled technique are optimized so that the fabricated QDs are as homogenous as possible. Still, QDs with different sizes always exist in real QD structures. As seen from (5.6), the size of the QD affects the energy states significantly. In addition to this, the luminescence intensity of the QD energy states has usually been lower compared to QW structures, for example. First, this was attributed to the reduced material quality resulting in the fabrication process of the QDs. However, this poor luminescence can result from the relaxation processes of the charge carriers. This phenomenon is the phonon bottleneck of charge carriers, as discussed earlier. In order to observe luminescence from QDs, charge carriers first have to relax close to the QD energy state minima. In general, the charge carriers can relax in the energy band minima with many relaxation mechanisms. The most usual mechanisms are via Coulomb interaction and Auger process, and the relaxation induced by an interaction with a phonon. To explain the inefficiency of the QD luminescence it has been suggested that the relaxation of charge carriers is a significantly slower process in QDs than in QW and bulk materials due to the more discrete energy states of QDs. Scattering occurs mainly via Auger and Coulombic processes. The relaxation processes via the phonons are more improbable in QDs since only few phonons have suitable energies for interaction (Jussila 2010).

5.1.5 Superlattice Heterostructure

Superlattice is a periodic structure of layers of two (or more) materials. Typically, the thickness of one layer is several nanometers. It can also refer to a lower-dimensional structure such as an array of quantum dots or quantum wires. If the superlattice is made of two semiconductor materials with different band gap, each quantum wells sets up a new set of selection rules which affects the conditions for charges to flow through the structure. The two different semiconductor materials are deposited alternately on each other to form a periodic structure in the growth direction. Since the first proposal of synthetic artificial superlattices in 1970, great advances in the physics of such ultra-fine semiconductors, presently called quantum structures, have been made. The concept of quantum confinement has led to the

observation of quantum size effects in isolated quantum-well heterostructures and is closely related to superlattices through the tunneling phenomena. Therefore, these two ideas are often discussed on the same physical basis, but each field has its own intrigue and different physics useful for applications in many electric and optical devices (GoldenMap 2013).

Semiconductor superlattices exhibit the resonant tunneling of carriers under the applied bias. This tunneling results from the overlay of the electron waves in the bound states of the periodic potential wells. This overlay can either occur among the bound states at the same energy level, or it can occur when the bound states become degenerate among the excited energy levels (in the case of sequential tunneling). The tunneling process was reported in the case of Zener diodes and Tunnel diodes in 1950s, whereas in the case of superlattices, it became apparent after the significant advancements in the growth procedures, such as molecular-beam epitaxy (MBE). The use of this procedure, along with its in situ analysis, a precise control over the thickness and composition of thin semiconductor layers can be achieved. The carrier transport measurements performed in GaAs–AlGaAs-based double barrier structure, and GaAs–AlAs-based superlattice structure showed the tunneling at specific bias amplitudes which coincide with the quantum-confined states (Younis 2010).

The superlattice miniband structures depend on the heterostructure type, called type I, type II and type III. For the type I heterostructures the bottom of the conduction band and the top of the valence sub-band are formed in the same semiconductor layer. In the type II the conduction and valence sub-bands are staggered in both real and reciprocal space, so that electrons and holes are confined in different layers. Type III superlattice involves semimetal material, one example is HgTe/CdTe superlattice. Although the bottom of the conduction sub-band and the top of the valence sub-band are formed in the same semiconductor layer in type III superlattice, which is similar with Type I superlattice, the band gap of type III superlattice can be continuously adjusted from semiconductor to zero band gap material and to semimetal with negative band gap. There also exists a class of quasiperiodic superlattices named after Fibonacci. A Fibonacci superlattice can be viewed as a one-dimensional quasicrystal, where either electron hopping transfer or on-site energy takes two values arranged in a Fibonacci sequence (GoldenMap 2013).

Semiconductor materials, which are actually used to fabricate the superlattice structures, may be divided by the element groups, IV, III–V and II–VI. While the group III–V semiconductors have been extensively studied, group IV heterostructures such as the Si_xGe_{1-x} system are much more difficult to realize because of the large lattice mismatch. Nevertheless, the strain modification of the sub-band structures is interesting in these quantum structures and has attracted much attention. So far mostly the III–V compound semiconductors represented by

the GaAs/Al_xGa_{1-x}As heterostructures have been investigated. In particular, one distinguished merit of the GaAs/AlAs system is that the difference in lattice constant between GaAs and AlAs is very small. In addition, the difference of their thermal expansion coefficient is also small. Thus, the strain remaining at room temperature can be minimized after cooling down from the higher epitaxial growth temperatures. The first compositional superlattice was realized using the GaAs/Al_xGa_{1-x}As material system. Superlattices can be produced using various techniques, but the most common are MBE and sputtering. With these methods, layers can be produced with thicknesses of only a few atomic spacing. In these highly sophisticated growth technologies chemical compositions and thicknesses of a material are controlled precisely under high vacuum. These material structures are grown by atomic/molecular interactions with the crystalline surfaces; and thin layers can be easily grown with a thickness of 2.8 Å, i.e., a monolayer (ML). In these heterostructures, where the layer thicknesses are comparable to the electron/hole wavelengths, the interlayer carrier interactions are apparent. These interactions of carriers with the potential energy barriers result in resonant tunneling. Resonant tunneling is a quantum effect in which the carrier transport through the barrier layers is transparent, which results in the formation of sub/mini bands in the superlattice region. The MBE technology as a means of fabricating semiconductor superlattices is of primary importance. In addition to the MBE technology, metal-organic chemical vapor deposition (MOCVD) has also contributed to the development of superconductor superlattices, which are composed of quaternary III–V compound semiconductors like InGaAsP alloys. Moreover, a combination of gas-source handling and ultrahigh vacuum (UHV) technologies such as metal-organic molecules as source materials, is becoming popular as well as gas-source MBE using hybrid gases such as arsine (AsH_3) and phosphine (PH_3) (GoldenMap 2013).

The motion of charge carriers in a superlattice is different from that in the individual layers: mobility of charge carriers can be enhanced, which is beneficial for high-frequency devices, and specific optical properties are used in semiconductor lasers. If an external bias is applied to a conductor, such as a metal or a semiconductor, typically an electrical current is generated. The magnitude of this current is determined by the band structure of the material, scattering processes, the applied field strength, as well as the equilibrium carrier distribution of the conductor. A particular case of superlattices called superstripes are made of superconducting units separated by spacers. In each miniband the superconducting order parameter, called the superconducting gap, takes different values producing a multi-gap, or two-gap or multiband superconductivity. Besides, artificial two-dimensional crystals can also be viewed as a 2D/2D case (2D modulation of a 2D system) and other combinations are experimentally available: an array of quantum wires (1D/2D) or 3D/3D photonic crystals (GoldenMap 2013).

5.2 Semiconductor Materials and Fabrication Process for Waveguides

Semiconductor waveguides are generally made from elements of III–V, II–VI, or IV–VI and so on. Historically, the III–V compounds have been the first and mostly used for optoelectronic device applications, such as GaAs and InP. Compared to Si and Ge, GaAs and InP have high electron mobility and velocities, properties that are extremely important for the development of high speed electronic devices. Their direct band gaps and therefore their high radiative efficiency make them important for optoelectronic materials. An attractive feature of the binary compounds is that they can be combined or alloyed to form ternary or quaternary compounds, or mixed crystals. These compounds are made up of three or four group III and group V atoms and by choosing different binary compounds, it is possible to select different band gaps and therefore varying emission energies for light sources. A wide range of compound semiconductors can be exploited to access a wide range of output wavelengths. However, by alloying it is possible to vary the band gap continuously and monotonically and together with it the band structure, electronic, and optical properties. The formation of ternary and quaternary compounds of varying band gaps also enables the formation of heterojunctions, which have become essential for the design of high performance electronic and optoelectronic devices. Among the common GaAs and InP-based ternary and quaternary compounds, the properties of $Al_xGa_{1-x}As$ have been most thoroughly investigated. Besides, there are $In_xGa_yAl_{1-x-y}As$ and $In_{1-x}Ga_xAs_yP_{1-y}$ that usually grown on InP substrates. The quaternary compounds have emerged as being extremely important as sources for optical fiber communication, since their band gaps correspond to the special window in which silica fibers have their lowest loss (at 1.55 μm) and minimal dispersion (at 1.3 μm). GaAs/AlGaAs waveguides provide interesting optical properties for nonlinear optical signal processing. In addition to the band-gap engineering capability, GaAs/AlGaAs has excellent electro-optic properties. The optical Kerr coefficient of GaAs is approximately 4 times larger than that of crystalline silicon, which can relax fabrication processes, and facilitate coupling to the fiber (Simatupang 2009).

Moreover, porous silicon waveguides provide an interesting alternative to conventional silicon-on-insulator (SOI) structures that could offer advantages for silicon interconnects modulators and components. Porous silicon is a nanoscale composite material with an effective refractive index between that of air and silicon that can easily be fabricated in multilayer structures (Apiratikul 2009).

With integrated optics, high-index contrast semiconductor waveguides provide exciting new opportunities to both study basic nonlinear optics in these materials as well as investigate new photonic devices such as Raman lasers and chemical sensors. Unlike a standard optical fiber (characterized by a core-cladding index difference of 0.01) in which most laser-induced fluorescence or Raman scattering will be lost out of the fundamental waveguide mode, in a high-index-contrast waveguide (characterized by a core-cladding index difference as high as 2.5),

most of the emitted Stokes-shifted light will be captured into a propagating mode. This property, coupled with the long interaction lengths provided by waveguides, make integrated high-index contrast semiconductor waveguides extremely efficient sources for optical experiments in which a pump laser induces signal light at a Stokes-shifted wavelength. In addition, the strong evanescent fields inherent in air-clad submicron waveguides make these systems intriguing candidates for chemical sensing based on fluorescence or Raman scattering from adsorbed analyte species (NRL 2013).

5.2.1 Silicon Waveguides

Silicon is an especially useful material for photonic components because it is transparent at the infrared wavelengths at which optical communication systems operate. Therefore, silicon waveguides have been primarily operated at wavelengths in the near-infrared (NIR), typically around 1.4–1.6 μm. This is convenient due to the large number of commercial optical components available in this regime (Spott et al. 2010). The silicon is usually patterned with sub-micrometer precision, into microphotonic components. These operate in the infrared, most commonly at the 1.55 μm wavelength used by most fiber-optic telecommunication systems. For instance, the silicon can typically lie on top of a layer of silica in what is known as SOI. That is, silicon photonic devices can be made using existing semiconductor fabrication techniques, and because silicon is already used as the substrate for most integrated circuits, it is possible to create hybrid devices in which the optical and electronic components are integrated onto a single microchip (Ganguly and Rahul 2011). Moreover, silicon waveguides have been investigated to provide faster data transfer both between and within microchips.

The propagation of light through silicon devices is governed by a range of nonlinear optical phenomena including the Kerr effect, the Raman effect, two photon absorption (TPA) and interactions between photons and free charge carriers. The presence of nonlinearity is of fundamental importance, as it enables light to interact with light, thus permitting applications such as wavelength conversion and all-optical signal routing, in addition to the passive transmission of light. Silicon waveguides are also of great academic interest, due to their ability to support exotic nonlinear optical phenomena such as soliton propagation (Zhang et al. 2007).

As silicon is transparent to infrared light with wavelengths above about 1.1 μm, and also has a very high refractive index, of about 3.5, the tight optical confinement provides by this high index allows for microscopic optical waveguides, which may have cross-sectional dimensions of only a few hundred nanometers. This is substantially less than the wavelength of the light itself, and is analogous to a subwavelength-diameter optical fiber. Single-mode propagation can be achieved, thus (like single-mode optical fiber) eliminating the problem of modal dispersion. The strong dielectric boundary effects that result from this tight confinement substantially alter the optical dispersion relation. By selecting the waveguide

geometry, it possible to tailor the dispersion to have desired properties, which is of crucial importance to applications requiring ultrashort pulses (Dekker et al. 2008). In particular, the group velocity dispersion (GVD) (that is, the extent to which group velocity varies with wavelength) can be closely controlled. In bulk silicon at 1.55 μm, the GVD is normal in that pulses with longer wavelengths travel with higher group velocity than those with shorter wavelength. By selecting suitable waveguide geometry, however, it is possible to reverse this, and achieve anomalous GVD, in which pulses with shorter wavelengths travel faster. Anomalous dispersion is significant, as it is a prerequisite for soliton propagation, and modulational instability (Agrawal 1995). In order for the silicon photonic components to remain optically independent from the bulk silicon of the wafer on which they are fabricated, it is necessary to have a layer of intervening material. This is usually silica, which has a much lower refractive index (of about 1.44 in the wavelength region of interest), and thus light at the silicon–silica interface will (like light at the silicon–air interface) undergo total internal reflection, and remain in the silicon. This construct is so called SOI as mentioned earlier. It is named after the technology of SOI in electronics, whereby components are built upon a layer of insulator in order to reduce parasitic capacitance and so improve performance (Celler and Cristoloveanu 2003). Silicon has a focusing Kerr nonlinearity, in that the refractive index increases with optical intensity. This effect is not especially strong in bulk silicon, but it can be greatly enhanced by using a silicon waveguide to concentrate light into a very small cross-sectional area. This allows nonlinear optical effects to be seen at low powers. The nonlinearity can be enhanced further by using a slot waveguide, in which the high refractive index of the silicon is used to confine light into a central region filled with a strongly nonlinear polymer (Koos et al. 2007). Kerr nonlinearity underlies a wide variety of optical phenomena. One example is four wave mixing, which has been applied in silicon to realize both optical parametric amplification and parametric wavelength conversion. Kerr nonlinearity can also cause modulational instability, in which it reinforces deviations from an optical waveform, leading to the generation of spectral-sidebands and the eventual breakup of the waveform into a train of pulses (Nicolae et al. 2006). Another example is soliton propagation. The evolution of light through silicon waveguides can be approximated with a cubic nonlinear Schrödinger equation, which is notable for admitting sech-like soliton solutions. These optical solitons (which are also known in optical fiber) result from a balance between self phase modulation (which causes the leading edge of the pulse to be red-shifted and the trailing edge blue-shifted) and anomalous GVD (Dekker et al. 2008; Agrawal 1995).

Silicon exhibits TPA, in which a pair of photons can act to excite an electron–hole pair. This process is related to the Kerr effect, and by analogy with complex refractive index, can be thought of as the imaginary part of a complex Kerr nonlinearity. At the 1.55 μm telecommunication wavelength, this imaginary part is approximately 10 % of the real part. The influence of TPA is highly disruptive, as it both wastes light, and generates unwanted heat. It can be mitigated, however, either by switching to longer wavelengths (at which the TPA to Kerr ratio drops), or by using slot waveguides (in which the internal nonlinear material has a lower TPA to

Kerr ratio). Alternatively, the energy lost through TPA can be partially recovered by extracting it from the generated charge carriers (Dekker et al. 2008; Bristow et al. 2007). The free charge carriers within silicon can both absorb photons and change its refractive index. This is particularly significant at high intensities and for long durations, due to the carrier concentration being built up by TPA. The influence of free charge carriers is often (but not always) unwanted, and various means have been proposed to remove them. One such scheme is to implant the silicon with helium in order to enhance carrier recombination. A suitable choice of geometry can also be used to reduce the carrier lifetime. Rib waveguides (in which the waveguides consist of thicker regions in a wider layer of silicon) enhance both the carrier recombination at the silica–silicon interface and the diffusion of carriers from the waveguide core. A more advanced scheme for carrier removal is to integrate the waveguide into the intrinsic region of a PIN diode, which is reverse biased so that the carriers are attracted away from the waveguide core. A more sophisticated scheme still, is to use the diode as part of a circuit in which voltage and current are out of phase, thus allowing power to be extracted from the waveguide. The source of this power is the light lost to TPA, and so by recovering some of it, the net loss (and the rate at which heat is generated) can be reduced (Dimitropoulos et al. 2005; Jones et al. 2005). Free charge carrier effects can also be used constructively, in order to modulate the light. Silicon exhibits the Raman effect, in which a photon is exchanged for a photon with a slightly different energy, corresponding to an excitation or a relaxation of the material. Silicon's Raman transition is dominated by a single, very narrow frequency peak, which is problematic for broadband phenomena such as Raman amplification, but is beneficial for narrowband devices such as Raman lasers. Consequently, all-silicon Raman lasers have been fabricated (Ganguly and Rahul 2011).

Silicon optical interconnects require the integration of a range of technologies. Firstly, an on-chip laser source is required. One such device is the hybrid silicon laser, in which the silicon is bonded to a different semiconductor (such as indium phosphide) which acts as the lasing medium. Another possibility is the all-silicon Raman laser, in which the silicon itself acts as the lasing medium. There must also be a means to modulate the light, thus causing it to carry data in the form of optical pulses. One such technique is to control the density of free charge carriers, which alter the optical properties of the waveguide. Modulators have been constructed where the light passes through the intrinsic region of a PIN diode, into which carriers can be injected or removed by altering the polarity of an applied voltage. By using an optical ring resonator with a built in PIN diode, data transmission rates of 18 Gbit/s have been achieved. By constructing devices where the electrical signal co-moves with the light, data rates of 30 Gbit/s have been achieved. By constructing devices where the multiple wavelengths are used to scale the modulation capacity 50 Gbit/s has been achieved. After passage through a silicon waveguide to a different chip (or region of the same chip) the light must be detected, converting the data back into electronic form. Detectors based on metal–semiconductor junctions (with germanium as the semiconductor) have been integrated into silicon waveguides. Moreover, silicon–germanium avalanche photodiodes capable of

operating at 40 Gbit/s have been fabricated. Complete transceivers have been developed and successfully commercialized in the form of active optical cables (Narasimha et al. 2008).

In addition, the choice of silicon as a substrate for the fabrication of optical waveguides follows naturally from its domination of microelectronics. It is important to note that no single material possesses the optimum properties for each individual device found in an IC, but silicon contains a base material from which all the required devices can be fabricated. This flexibility is also important in the fabrication of silicon-based, planar light wave circuits (PLCs). Many of the optical properties of silicon would suggest it to be an ideal material for PLC fabrication. It is virtually transparent to the important telecom wavelengths around 1,550 nm. Further, silicon dioxide (SiO_2) shares its chemical composition with glass fiber, providing a degree of compatibility. Silicon has a relatively high refractive index around 3.5, compared to that for fiber (around 1.5) which allows the fabrication of submicron dimensional waveguides in the SOI system. SOI's large refractive index contrast imposes design constraints on single-mode rib waveguides; however, it can also be considered an advantage. It makes possible core sizes much smaller than 1 μm, which in turn makes possible very compact integrated optical devices with waveguide bending radii as small as a few microns. Silicon layer thicknesses below about 250 nm are required for slab waveguides to be unconditionally single mode. When two-dimensional waveguides are patterned in such thin silicon, a guide with a width of a few hundred nanometers is typically defined by etching away the surrounding silicon all the way down to the SiO_2 substrate and then depositing a layer of SiO_2 or a transparent polymer to embed the silicon. The result is a photonic wire surrounded on all sides by a low-index medium. The small dimensions of photonic wires are conceptually very attractive for on-chip optical interconnects and integrated optical devices with small footprints. However, they are very demanding in terms of fabrication technology. Conventional optical lithography (with illumination wavelengths of 300 nm or more) cannot provide the required resolution. Electron-beam lithography provides the necessary accuracy, but it is not well suited for mass production because it is a serial process. For this, nanophotonic waveguides using the available tools of advanced CMOS fabrication based on deep ultraviolet (UV) lithography have been fabricated (Knights and Jessop 2007).

On the other hand, porous silicon offers an interesting alternative to conventional silicon structures that could offer advantages for silicon interconnects, modulators and components. Porous silicon is fabricated by electrochemical etching of crystalline silicon, which produces a nanoporous skeleton comprised of silicon and air. The typical pore size formed in this process ranges from 5 to 100 nm, depending on the etching chemistry and substrate doping. Because the pores are smaller than the optical wavelength, porous silicon behaves like an effective medium with refractive index between that of air and silicon. The refractive index depends on the porosity, which can be controlled by adjusting the electrochemical current density. Complex multilayer porous structures can be fabricated by varying the current density during fabrication. Optoelectronic devices based on porous silicon including waveguides, LEDs, photodetectors, passive

optical filters, microcavities, sensors and optical switches have been developed. In addition to the flexibility of a controllable refractive index, porous silicon has a number of unique properties that make it attractive for modulators and sensors. It is electrically conductive in the direction perpendicular to the surface, while being optically transparent for signals polarized parallel to the surface, which could facilitate optoelectronic connectivity. In addition, the large internal surface area of porous silicon increases the surface recombination rate, which dramatically reduces the free-carrier lifetime (Apiratikul 2009).

There has been a great deal of success in attempts to monolithically fabricate the vast majority of components required in an optical system such as waveguides, modulators, (de)multiplexers, and detectors on a silicon substrate. However, the outstanding limitation of silicon in the photonics arena is its indirect band gap that prevents the straightforward formation of efficient optical sources. Indeed, the search for silicon-based optical source forms the greatest challenge to the widespread dominance of silicon in optoelectronics. Although not yet dominant as a material for optoelectronic fabrication, it is difficult to imagine highly integrated devices of any kind not based on silicon technology. The next few decades will likely witness the increased migration of silicon photonics from the research laboratory to the manufacturing facility with benefit to areas as diverse as microelectronics, telecommunications, and the biological, environmental, and medical sensor industries (Knights and Jessop 2007).

5.2.2 *Gallium Arsenide Waveguides*

GaAs/AlGaAs waveguides provide interesting optical properties for nonlinear optical signal processing. The optical Kerr coefficient (nonlinear refractive index) n_2 of GaAs is approximately 4 times larger than that of crystalline silicon and three orders of magnitude larger than that of standard optical fiber. Table 5.1 compares parameters such as propagation loss (α), optical Kerr coefficient (n_2) and nonlinear parameter (γ) of some of the nonlinear waveguides that have been proposed for optical signal processing. One of the parameters used to evaluate the efficiency of third-order-nonlinearity-based waveguide devices is the nonlinear parameter γ, which depends not only on material nonlinearity (n^2) but also on the geometry of the waveguide. γ is defined as (Apiratikul 2009).

$$\gamma = \frac{2\pi n_2}{\lambda A_{\text{eff}}} \tag{5.7}$$

where λ is the signal wavelength, and A_{eff} is the effective area of the waveguide. For nanoscale semiconductor waveguides, this nonlinear factor (γ) has to be redefined to take into account the tensor nature of the third-order nonlinear susceptibility, the direction of propagation relative to the crystal axes and the vector nature of the electromagnetic mode, including nonzero z-components of the electric field. The

Table 5.1 Comparison among parameters in nonlinear waveguide devices (Apiratikul 2009)

Waveguide devices	Propagation loss (dB/cm)	Optical Kerr coefficient (cm^2/W)	Effective area of the waveguide (μm^2)	Nonlinear factor (1/(Wm))
Standard fiber (SMF-28)	5×10^{-7}	2.2×10^{-16}	80	1.1×10^{-3}
Bismuth-oxide fiber	3×10^{-2}	8.2×10^{-15}	3	1.1
Chalcogenide fiber taper	1.7	1.1×10^{-13}	0.64	68
Chalcogenide waveguide	0.2	3×10^{-14}	7.2	1.7
Organic χ^3 in slot waveguide	23	8.2×10^{-15}	0.1	104
Silicon nanowire	3.6	4.5×10^{-14}	0.14	130
AlGaAs nanowire	82.5	1.5×10^{-13}	0.3	202
GaAs ridge waveguide	4–6	2.9×10^{-13}	1.8	64

nonlinear efficiency could be improved by using a material with large nonlinearity or by reducing the guided-mode area of the waveguides. In addition to the nonlinearity parameter (λ), another figure of merit that has been used to compare the nonlinearity in different materials and waveguides is FOM_{2PA}. FOM_{2PA} takes into account the TPA loss (β_{2PA}) in addition to the nonlinearity (Apiratikul 2009)

$$FOM_{2PA} = \frac{n_2}{\lambda \beta_{2PA}} \tag{5.8}$$

The GaAs/AlGaAs material system could be designed to achieve a large FOM_{2PA}. This material system allows for band-gap engineering: by adding Al into AlGaAs, the energy band gap of AlGaAs can be altered. For example, the band gap energy of AlGaAs can be designed such that the photon energy of the optical signal at communication wavelengths falls below the half-band gap, thus avoiding TPA, while maintaining a large optical Kerr coefficient. GaAs waveguides could also allow for integration of nonlinear optical devices with optically active devices such as lasers, amplifiers, detectors and modulators. A variety of GaAs/AlGaAs waveguide devices have been developed, including directional couplers, microring resonators and photonic crystal cavities. In addition, GaAs and AlGaAs nanowire waveguides have been investigated. For example, a cross-section as small as 0.2 μm^2 was achieved with the linear propagation loss of approximately 50 dB/cm, which is still too high for practical nonlinear applications; GaAs/AlGaAs waveguides with an effective area of 0.4 μm^2 were demonstrated with propagation loss as low as 0.9 dB/cm at 1,550 nm (Shin et al. 2009).

Figure 5.5a shows a cross-section of the material layer of GaAs/AlGaAs waveguide structure. Its epistructure was grown by MBE on a n-GaAs substrate. The structure comprises a 0.8-μm-thick GaAs guiding layer surrounding by a 1-μm-thick $Al_{0.2}Ga_{0.8}As$ upper cladding and a 3.5-μm-thick $Al_{0.2}Ga_{0.8}As$ lower cladding. The layer thicknesses were to ensure single-mode operation and to minimize leakage loss to the substrate. This structure was used both for making a P–I–N waveguide photodetector, and for a passive waveguide. Both parts of the top and

bottom cladding layers, which are close to the core, are left undoped in order to help suppress free-carrier absorption (FCA) loss. A 2.4-μm wide ridge waveguide was fabricated in a single photolithography step. First, a 2,000-nm positive photoresist (PR1-2000A) was spin on a small cleaved sample (typically 1.5 cm × 1.5 cm). Next, the waveguide patterns were exposed using UV contact photolithography with a clear field mask. The waveguides were then etched to a depth of 1.8 μm via inductively coupled plasma (ICP) etching with gas mixtures of BCl_3 and Cl_2. For this process, the BCl_3 and Cl_2 flow rates were controlled to be 12.5 and 2.5 sccm, respectively, with a chamber pressure of 1 mTorr at a substrate temperature of 25± °C. Two RF sources (70 and 500 mW) were used to generate high-density plasma and to introduce a self-biased electrical field, respectively. With two RF power sources, the ICP system has the flexibility to control ion density and ion energy independently, unlike a conventional reactive ion etching system. These etching parameters are optimized to create a vertical etch profile with the smooth sidewalls required for a low-loss waveguide. For these parameters, the ICP etch rate was estimated to be 300–350 nm/min with a GaAs:photoresist selectivity of 3:1. Figure 5.5b depicts a cross-sectional schematic illustration and a scanning electron micrograph of a GaAs/AlGaAs waveguide. The calculated TE mode contours were superposed on the cross-section in Fig. 5.5b with the effective area A_{eff} estimated to be 1.8 μm^2, based on the calculated mode. During the ICP etching process, a thin layer of photoresist byproducts containing Cl–C–H polymers is deposited on the top and sidewalls of the waveguides. These residual polymers are difficult to remove with standard solvent cleaning using acetone, methanol and isopropanol. The sample is dipped into H_3PO_4 at room temperature for 2 min immediately after the ICP etch, followed by O_2 plasma cleaning in a reactive ion etching (RIE) system for 5 min and solvent-based (NMP) stripping at 70± C for 15 min to remove the residue. The sample substrate is then thinned down to 120 μm to facilitate accurate cleaving. After that, the sample is scribed using high-power laser scriber setup and is cleaved on the cleave stage on both facets to a length of 4.5 mm. Finally, a silicon nitride antireflection (Si_3N_4-AR) coating was deposited on both facets of the waveguide by high-density chemical vapor deposition (HDCVD). First, ammonia (NH_3) is deposited for 3 min to improve the adhesion between the Si_3N_4 film and GaAs. Then, Si_3N_4 was deposited with gas mixtures of N_2 and SiH_4 with RF power of 500 W under the chamber pressure of 5 mTorr at 300± C. Both N_2 and SiH_4 flow rates were controlled to be 10 sccm. Under this condition, the deposition rate for the horizontal surface was measured to be approximately 34–37 nm/min. The Si_3N_4 film has a refractive index n of 2 at the wavelength of 1,550 nm. For a single layer AR coating, a quarter-wavelength-thick Si_3N_4 film is deposited at both facets of the waveguide. A quarter-wavelength thick film is chosen in order to minimize the normal incidence reflection. For applications operating at the wavelength of 1,550 nm, the target Si_3N_4 thickness is calculated to be $l/4 = 194$ nm. The deposition time is calculated by taking into account that the deposition rate on vertical surfaces, like the waveguide facets, is approximately 50 % slower than on horizontal surfaces. After AR-coating, the sample is mounted to the submount and is ready to be tested (Apiratikul 2009).

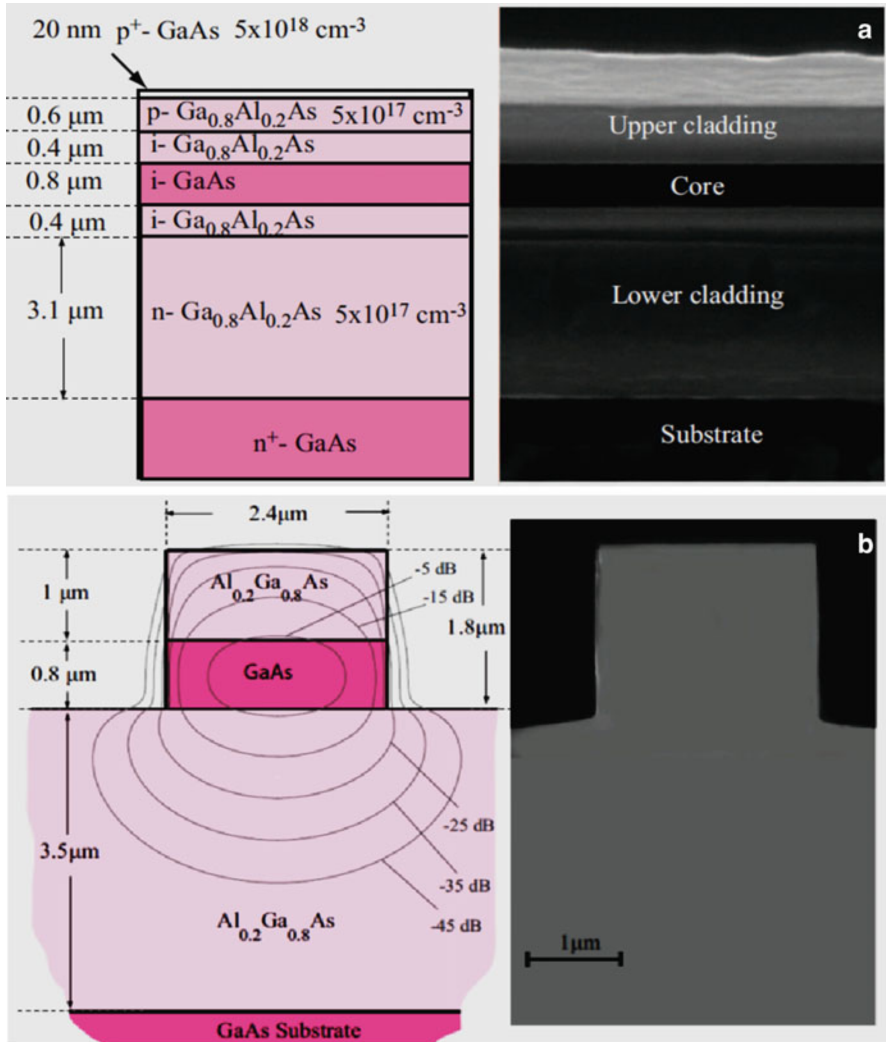

Fig. 5.5 Schematic cross-section and scanning electron micrograph of material structure for a GaAs/AlGaAs optical waveguide (Apiratikul 2009): (**a**) Cross-section of a GaAs/AlGaAs waveguide. (**b**) Schematic illustration with calculated fundamental TE mode profile (contours labeled in dB relative to peak value)

5.2.3 InAs Quantum Dots

As shown in Fig. 5.6, InAs QD structures can be grown on 500 µm-thick semi-insulating (100) InP substrates (Apiratikul 2009): (a) 100-nm thick InP buffer layer was grown on the substrate with a V/III ratio of 220, a growth temperature of 640 °C, and a growth time of 450 s. Then, InAs island layer was grown on the InP

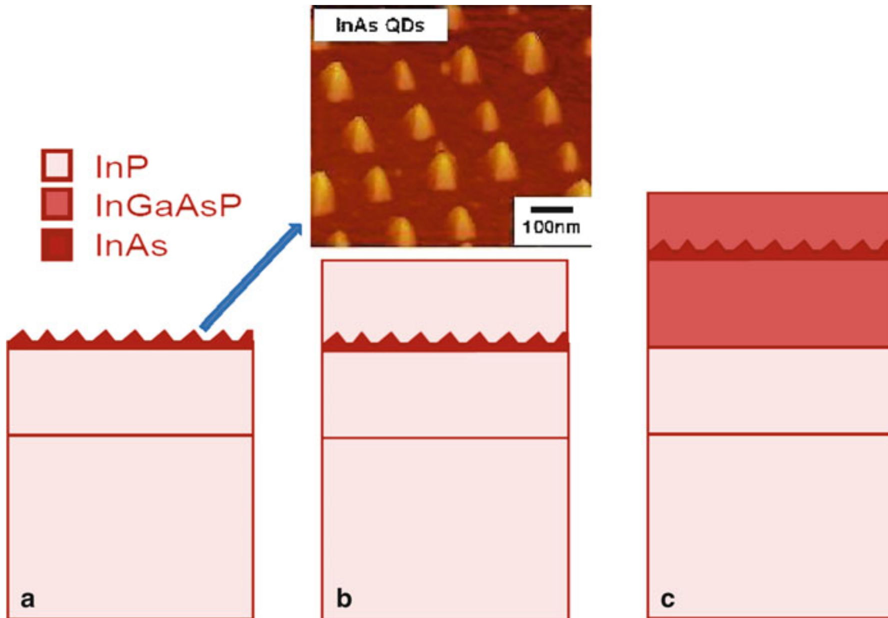

Fig. 5.6 Cross-section of the fabricated InAs quantum dot samples (Apiratikul 2009): (**a**) InAs/InP island structure, (**b**) InAs/InP QD structure, and (**c**) InAs/InGaAsP/InP QD structure

buffer layer with a V/III ratio of 12. The growth temperature and growth time of this layer were changed between 420 and 550 °C, and between 1.25 and 8.25 s, respectively. The schematic structure of these samples is shown in Fig. 5.6a. (b) 100-nm thick InP buffer layer was grown on the substrate with the same growth parameters as in (a). Then, an InAs layer was grown on the InP buffer layer at the temperature of 520 °C. The growth time of the layer was between 1.25 and 10.6 s. After this, the InAs layer was capped with a 50-nm thick InP layer. The InP capping layer was grown at the same temperature as the InAs layer. This was performed to avoid unnecessary temperature ramping which was evaluated to cause more harm than the relatively low growth temperature of InP. The schematic structure of these samples is shown in Fig. 5.6b. (c) 100-nm thick InP buffer layer was again grown with the same growth parameters as in (a) and (b). Then, a 100-nm thick $In_xGa_{1-x}As_yP_{1-y}$ barrier layer was grown on the InP barrier layer with a V/III ratio of 120, a growth temperature of 640 °C and a growth time of 350 s. The aim was to grow the InGaAsP layer as lattice-matched to InP as possible. After this, the InAs QD layer was grown on InGaAsP at 520 °C with a V/III ratio of 12 and a growth time of 2 s. Then, this InAs layer was capped with a 50-nm thick $In_xGa_{1-x}As_yP_{1-y}$ layer. This layer was grown at the same temperature as the InAs layer. The schematic structure of these samples is shown in Fig. 5.6c. Self-assembled growth of InAs islands on InP can be examined by fabricating two series of samples (structure of Fig. 5.6a). The nominal thickness and growth temperature

of the InAs layer can be varied in these series. In the first series, the nominal thickness of the InAs layer can vary from one monolayer (ML) to six MLs. The growth rate of InAs is higher at higher temperatures. In addition, the cooling down process also affects the island formation (Apiratikul 2009).

5.3 Quantum-Well Technology

The key to realize on-chip integrated optical devices is working with a low-loss, highly nonlinear material system that allows the creation of both active and passive photonic devices. With quantum-well technology, III–V group semiconductors, such as GaAs and its alloys, can be used to create low-loss waveguides with very high second and third-order nonlinearities, or direct band gaps that enable the fabrication of bright lasing sources. For example, AlGaAs-based heterostructures such as superlattices and MQWs allow for tailoring the linear and nonlinear optical and electronic properties of the devices to suit the given application requirements. GaAs:AlGaAs MQW structures can efficiently confine free carriers in the lower-energy gap layers, and hence enable the fabrication of efficient laser sources. Superlattices allow control over the devices' band gap and tailoring it to the required application. This band structure is characterized by the formation of minibands of allowed energy levels that are dependent on the composition of the superlattice constituents and the thickness of the barriers and wells. The band gap (the absorption edge) change directly alters the macroscopic refractive index through the Kramers–Kronig relations. The change in band gap alters the magnitude of the tensor elements of the second and third-order nonlinear susceptibilities (Sigal 2010).

5.3.1 Characterization of Quantum Well

The GaAs quantum well (~20 nm) with AlGaAs barriers and claddings, grown using MOCVD, was first used to achieve the room temperature injection laser action, which had the threshold current densities of ~3,000 A/cm^2. Later on, much work has been reported in quantum-well laser structure improvement. The graded index separate confinement heterostructure (GRIN-SCH) symmetric waveguide laser, grown using MBE, reported the threshold current density of 500 A/cm^2, and further improved it down to 160 A/cm^2. The GRIN-SCH structure, not only can achieve very low threshold current density but also the selection of GRIN layers can result in any desired far-field pattern. The minimum threshold current density can usually be achieved in short devices with a large number of quantum wells, and long devices with a small number of quantum wells. This is explained by the higher mirror loss for a shorter cavity, which requires a higher gain factor for the laser action to occur, and is provided by an increased number of quantum wells. The excitation wavelength can be varied as a function of decreasing GaAs quantum-

well width, bounded by 80 Å $Al_xGa_{1-x}As$ barriers. For instance, the pulsed excitation was observed in 10 and 20 GaAs quantum-well material systems, and a red shift of about 20 nm was reported. In a different material system which had 20 GaAs quantum wells (25 Å) bounded by $Al_{0.31}Ga_{0.69}As$ (40 Å) barriers, indicated coupling between the quantum confinements among the quantum wells. The excitation in this case also observed a red shift of 18 nm which was attributed to reabsorption (Younis 2010).

In addition, suspended quantum-well heterostructures have focused on lasing in photonic crystals, microcantilever photodetectors, and lateral band structure deformation. The successful fabrication of a suspended quantum-well waveguide in the III–V material system depends critically on the epitaxial strain, band structure, and etches selectivity of the different materials. With a proper choice of materials, alloy fractions, and layer thicknesses within the heterostructure, a suspended MQW waveguide can be fabricated to allow low-loss propagation in the optical L-band, just 125 nm below band gap. Such a design allows strong electro-optic effects in the near band edge regime due to the quantum-confined Stark effect, without adding significant interband absorption loss. InGaAs quantum wells with InGaAsP barriers grown on InP have been designed to have a band edge near 1,500 nm. Both InGaAs and InGaAsP (with a phosphorous content below about 60 %) are also known to have a high resistance to a hydrochloric acid (HCl) etch, which is used to selectively remove an InAlAs sacrificial layer. By growing either the InGaAs or InGaAsP layers with a small amount of tensile strain, the suspended waveguide will not crack or buckle upon release from the sacrificial layer. This 590 nm thick waveguide layer is grown on a 1.6 μm lattice-matched $In_{0.52}Al_{0.48}As$ sacrificial layer and a 50 nm thick InGaAs etch stop layer. The waveguides are patterned and etched using electron-beam lithography followed by a chlorine-based inductively ICP etch and then released by selectively etching the sacrificial layer, resulting in a MQW core surrounded by an air cladding. The waveguides are attached using tethers spaced at regular intervals along the waveguide length. The tethers vary in width from 2 to 4 μm while the waveguide width ranges from 1 to 6 μm on a given sample. The waveguide lengths range between 1.2 and 2.4 mm, and the tether spacing along the waveguide ranges between 120 and 575 μm. An example of such a waveguide is shown in Fig. 5.7. Figure 5.7a shows a fabricated waveguide 2 μm wide along with two tether pairs of the same width. Figure 5.7b shows a close-up of one of the facets of this waveguide. Suspended MQW waveguides can exhibit a propagation loss that is approximately 4 dB/cm at wavelengths of only 125–150 nm below band gap. Besides, tether losses can be as low as 0.15 dB per tether pair, permitting their use in devices that require multiple tethers in an active area. Epitaxial tensile strain ensures that the waveguides remain flat upon release. These waveguides, when fabricated with the MQW between P-doped and N-doped layers, should exhibit extremely high electro-optic coefficients due to the strong overlap between the small optical mode and the electrical bias field. Coupled or asymmetric MQWs should increase the electro-optic coefficients even further, enabling extremely low-drive voltage ($V\pi$) modulators in lengths of 1 mm or less. Forward biased P–I–N MQWs with band edges near 1,550 nm could be used as electroabsorptive

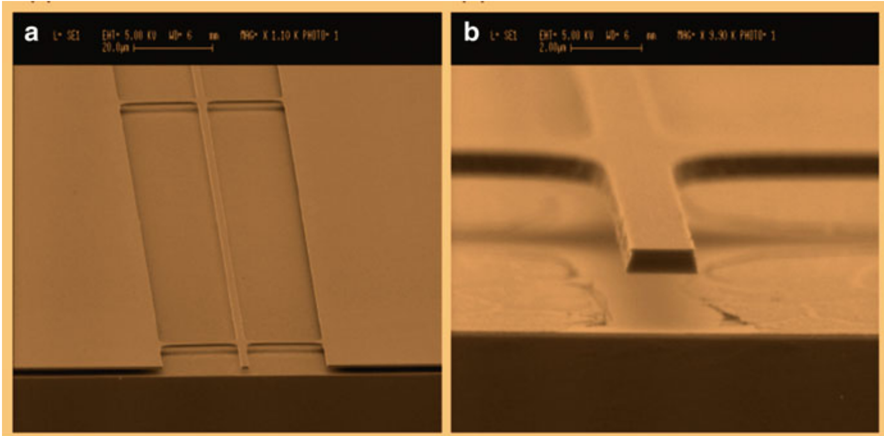

Fig. 5.7 An example of MQW waveguide (Stievater et al. 2008): (**a**) fabricated waveguide 2 μm wide along with two tether pairs of the same width; (**b**) a close-up of one of the facets of this waveguide

modulators, lasers, or amplifiers that could be integrated with suspended waveguide switches or sensors. In addition, since the waveguides can be surrounded by a low-index chemoselective coating after the sacrificial etch, the waveguides can act as chemical sensors (Stievater et al. 2008).

5.3.2 Quantum-Well Intermixing

The properties of MQWs and superlattices are highly desirable for implementing all-optical integrated devices. In order to implement a cost-effective multifunctional optical device on-chip a direct control over the optical properties of the material, and specifically the band gap, is necessary. Quantum-well intermixing (QWI) is a post-growth fabrication technique that allows modifying the band gap of a MQW or superlattice structure on the same wafer, and thus allowing the integration of smaller-band gap lasers with larger-band gap, lower-loss linear and nonlinear waveguides. QWI, in the simplest terms, is induced disorder in a MQW structure that happens due to the diffusion of MQW constituents between the barriers and wells. Even a small amount of such diffusion breaks the structure symmetry and changes the band gap of the structure back to its bulk value. The disordering, in turn, can be achieved by means of a mechanism called impurity-free vacancy disordering (IFVD), where no foreign impurities are introduced into the wafer and losses are minimized. Disorder is instead achieved by shallow As^+ ion implantation, which creates defects in the lattice. The implantation is followed by rapid thermal annealing (RTA) which enables the defects to diffuse across the superlattice and render the material as bulk. The controlled ion

implantation and subsequent RTA allows patterning the wafer before the etching process, making appropriate modifications to the wafer's band gap (and linear and nonlinear properties) to suit the application at hand. Such fabrication process has proven to introduce lower scattering losses than the Etch-and-Regrowth process for shallow-contrast waveguides (Younis 2010).

5.3.3 Micromachining

Micromachining technologies have the potential to dramatically enhance the functionality and performance of integrated photonic devices. For example, integrated switches based on deflection of a suspended waveguide have been demonstrated in SOI and gallium arsenide (GaAs) systems and in indium phosphide (InP)-based systems. However, the optically active nature of III–V semiconductors has yet to be fully exploited in these micromachined waveguide devices; Lasers, optical gain segments, or electro-optic modulators can be integrated with micromachined III–V waveguides. Not only would the use of electro-optically active heterostructures eliminate the need for off-chip photonic gain or modulation components but the electro-optic properties could also be enhanced by the unique optical properties of suspended semiconductor waveguides, which include high-index contrast and strong evanescent fields. The high-index contrast inherent in suspended waveguides enables small cross-sectional mode areas, which in turn enhance nonlinear optical and electro-optical properties. In addition, the evanescent fields in the air surrounding the waveguide suggest uses in sensing that could also take advantage of integrated gain segments (Stievater et al. 2008).

5.4 Doped Semiconductor Waveguides

Many lanthanide elements have played an important role in various optoelectronic and photonic applications, ranging from emitting elements in solid-state lasers (for example the Nd:YAG laser) and in phosphors for color lamps and displays (for example Eu and Tb) to optical waveguides (using Er or Pr). These rare earth (RE) elements have a partially filled inner (4*f*) shell shielded from its surroundings by completely filled outer (5*s* and 5*p*) orbitals. Due to this shielding, the intra 4*f* shell transitions result in very sharp optical emissions at wavelengths from the ultraviolet to the infrared (IR). The wavelengths of these emission lines are determined by the energy of the transition between 4*f* states of the RE and are relatively independent of the host material. However, the host material does have a very strong effect on the radiative transition probability, in other words on the photoemission intensity. In general, RE-doped conventional semiconductors (Si, GaAs, etc.) have exhibited limited photoemission at room temperature due to low RE solubility and severe temperature quenching. The thermal quenching in Er-doped

semiconductors decreases with increasing band gap. Therefore, wide-band gap semiconductors (WBGS) are attractive hosts for RE elements. For instance, GaN is a WBGS that is intensely investigated for (intrinsic) optical and electronic applications. Er-doping of GaN was shown to produce strong near-IR 1.5-m emission suitable for fiber-optic telecommunications from the lowest excited state. Photoemission from higher excited RE states in GaN can cover the entire visible spectrum: light emission in the green (from Er at 537/558 nm), red (Pr at 650 nm, Eu at 621 nm), and blue (Tm at 477 nm). Emission in the NIR is also obtained at 801 nm from Tm, at 1,000 and 1,540 nm from Er, and at 956, 1,303, and 1,914 nm from Pr. The RE doping of GaN (as well as AlN and GaN) can be accomplished by ion implantation or by in situ doping during growth. Ion implantation has the advantage of a simple process and can control the doping concentration independent of the growth conditions. However, the implantation doping approach also has disadvantages: introduction of damage in the GaN (which cannot be completely removed by annealing, especially at the higher concentrations used in ELDs), and the inability to uniformly dope thick layers because of the limited penetration range of the heavy RE ions (Steckl et al. 2002).

5.4.1 In Situ RE Doping

In situ RE doping requires a good understanding and control of the overall growth process and of the interaction of the RE flux with the main V/III fluxes. However, once that is established, good control of the RE concentration over many orders of magnitude can be obtained and very uniform doping can be accomplished. Furthermore, in situ doping does not suffer from the damage effects of ion implantation and, hence, results in more efficient emission. For instance, REs can in situ introduced during growth of the GaN layer by MBE. RE doping of GaN represents an interesting alternative to semiconductor alloying (GaN/InN/AlN) for visible light-emission applications and has the additional attractive aspect of strong IR emission for telecommunications and other applications. Theoretically, RE intra-4*f* atomic transitions are parity forbidden by the Laporte selection rule. RE ions incorporated into a partially ionic solid favor substitutional occupation of the cation site. In addition to RE incorporation, the cation site must provide an uneven ligand crystal field in order to relax the selection rule and increase the probability of intra-4*f* transitions. These 4*f*–4*f* transitions, however, are still not fully allowed, resulting in excited state lifetimes of ~1 ms for RE-doped systems. In wurtzitic GaN, which has a significant component of ionic bonding, the RE ions have strong optical activity levels, since they are generally substitutionally located on the Ga sublattice where the lack of inversion symmetry produces strong ligand fields, thereby increasing the 4*f*–4*f* transition probability. These substitutional RE dopants are, therefore, likely to be the optically active RE centers observed in GaN:RE. The specific 4*f* transitions and associated emission wavelengths in GaN doped with Eu, Er, and Tm are shown in Fig. 5.8a. The dominant transitions producing visible

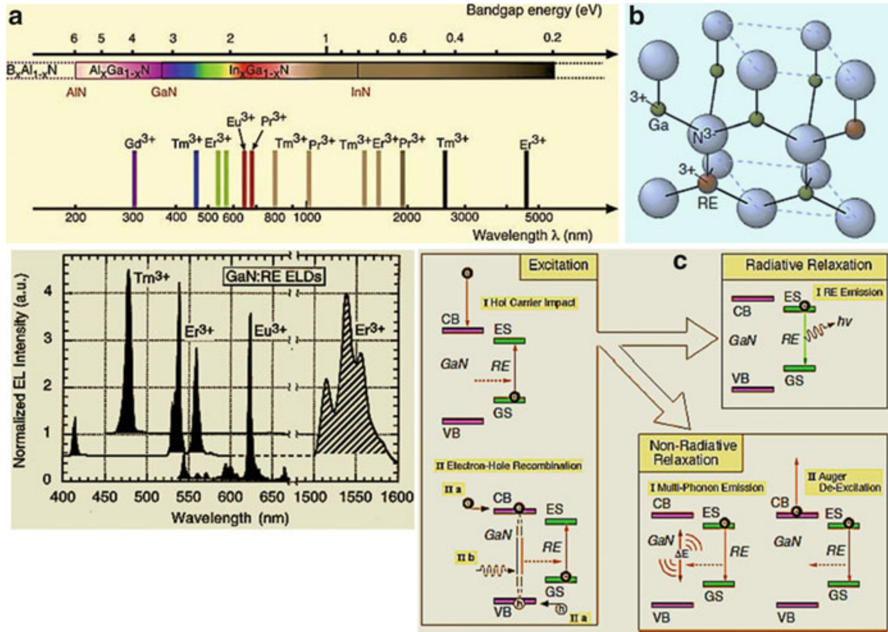

Fig. 5.8 RE-doped GaN photoemission (Steckl et al. 2002): (**a**) emission spectra from Tm-, Er-, and Eu-doped GaN ELDs and emission wavelengths from selected transitions in rare earth ions and associated band gap energies of III-N compound semiconductors; (**b**) bonding model for RE-doped GaN, with the RE ion located substitutionally on the Ga sublattice; (**c**) mechanisms for RE dopant excitation and relaxation in the GaN host

emission are indicated with thicker lines. A simple model of the GaN:RE crystal structure is shown in Fig. 5.8b. A strongly bonded GaN lattice, in conjunction with substitutional incorporation allows unusually high RE doping concentrations (up to 3–5 at.%), while preserving the optical activation of RE dopants. By comparison, the use of RE-doped II–VI semiconductors as emitters and phosphors suffers from a more weakly bonded lattice, and substitutional location of the RE ions on the two cation sites, which generates additional defects due to lack of charge neutrality. Rutherford back scattering (RBS) channeling analysis confirms that a great majority 95 % of the Er ions occupy substitutional sites on the Ga sublattice even at relatively high concentrations of 1 at.%. The Er–N bond has been measured by EXAFS analysis to be 2.17, versus a Ga–N bond length of 1.95. This unusually short Er-nearest neighbor bond length in GaN is thought to be due to two major factors (Steckl et al. 2002): (a) the low fourfold coordination, compared for example to a 12-fold coordination in ErSi; (b) a more polar bond for Er–N than for Ga–N (due to electronegativity differences), which helps to energetically compensate for the Ga–Er size mismatch. Light emission from GaN:RE has been demonstrated via photoluminescence (PL), cathodoluminescence (CL), and EL. The dominant mechanisms for excitation and subsequent relaxation of RE

dopants in GaN are depicted in Fig. 5.8c. In PL, electron–hole pairs are generated by above band-gap photon absorption, charge carrier generation is provided by a high-energy electron beam in CL, and in EL, carrier injection occurs by the application of bias voltage to electrical contacts on the GaN layer. The charge carrier energy is transferred to the RE dopants by impact excitation of hot carriers or as a result of nearby electron–hole recombination. The REs then experience either nonradiative relaxation (through multiphonon emission and/or Auger electron excitation) or radiative relaxation. The latter mechanism is the desired outcome as it results in the photoemission utilized in ELDs. The relative strength of the radiative relaxation mechanism is a complex function of the GaN crystalline quality and the RE concentration. For example, increasing the crystallinity of the GaN host reduces the concentration of point defects, and thus reduces the opportunity for RE nonradiative relaxation. However, high crystallinity is normally achieved under conditions which prevent the incorporation of the optimum RE concentration into the GaN layer. Further, for the case of above-band gap photo-pumping of highly crystalline RE-doped GaN, intrinsic (band-to-band) electron–hole recombination provides a high probability radiative intrinsic relaxation mechanism in competition with the RE radiative relaxation (Steckl et al. 2002).

In situ RE doping of GaN has resulted in the successful fabrication of ELDs with red, green, and blue (RGB) color emissions using Eu, Er, and Tm, respectively. The most crucial factors for obtaining and improving EL emissions include RE concentration, growth temperature, and stoichiometry (i.e., V/III ratio) of the host material. With regard to concentration, the EL emission increases more or less linearly with RE concentration at low levels. On the other hand, at high concentration levels, an emission quenching effect occurs due to an increase in RE–RE energy transfer, rather than radiative relaxation. Hence, there is an optimum RE concentration for which maximum emission is observed. Most phosphor systems exhibit this concentration quenching phenomenon. For example, ZnS:Mn exhibits its luminance maximum at 0.5–1.0 wt% of Mn. Growth temperature and Ga flux (V/III ratio) affect the RE emission through the properties of the GaN host (such as crystallinity and resistivity) and directly through their influence on RE incorporation. These three parameters, RE flux (determined by the RE cell temperature), growth (substrate) temperature, and Ga flux (determined by the Ga cell temperature) are externally controlled and adjusted during GaN:RE MBE growth. In general, all Er-doped host materials exhibit a practical limit in Er concentration beyond which the optical emission begins to decrease. The ultimate doping limit is the RE solid solubility in the host material. Concentrations which are introduced in a nonequilibrium process and which are larger than the solid solubility can result in the formation of a second phase material which contains some (or all) of the RE concentration. This precipitation is accompanied by the concomitant degradation of optical and electronic properties of the host material. A practical limit, which is usually reached first, has to do with the concentration quenching effect. For example, the solubility limit of Er in Si is $\sim 10^{18}/\mathrm{cm}^3$, while the PL intensity at 1.54 μm was to saturate at even lower concentration of $\sim 5 \times 10^{17}/\mathrm{cm}^3$, which represents an Er atomic percentage of only $\sim 10^{-3}$ at.%. Maximum Er concentration

is ~5 × $10^{18}/cm^3$ in GaAs and ~4 × $10^{19}/cm^3$ in Al_2O_3. Er concentration in GaN ranges from 0.025 to 10 at.% by varying the Er cell temperature from 740 to 980 °C. The Er concentration follows an exponential dependence on the Er cell temperature. An Arrhenius-like thermal activation energy estimated from this curve was 2.9 eV, which gives an excellent agreement with the activation energy of 3.0 eV for the Er vapor pressure in this temperature range. As the RE ion concentration is increased, the average distance between ions is reduced proportional to the cube root of the RE concentration. When RE ions are located sufficiently close to each other, the excitation residing in one ion can migrate to a neighboring ion of the same species as a result of resonant energy transfer. This process is known as cross-relaxation. The energy migration process increases the possibility that the excitation is dissipated at nonradiative sites, resulting in saturation or a decrease in optical emission. The optimum Er concentration is 1 at.%. The corresponding Er–Er spacing is estimated to be ~15 Å. On another hand, an MBE growth temperature in the neighborhood of 600 °C produces the optimum ELD emission intensity. In addition, RE optical emission from GaN films is a strong function of the ratio of the Ga- and N-bearing fluxes (V/III) during growth. The V/III ratio can be modified by changing either component, but is typically adjusted by controlling the Ga flux. The Ga flux is critical to GaN crystalline quality and good crystalline GaN is usually grown under slightly Ga-rich growth conditions. GaN crystallinity and intrinsic luminescence are strong functions of Ga flux during growth. Therefore, it is clear that the RE-related emission, which is dependent on the crystallinity of the GaN host, will also be strongly affected by the Ga flux. The optimum growth condition for Er optical activity is found under slightly N-rich flux near the stoichiometric region. Under these growth conditions, the resulting GaN crystallinity is high enough for efficient Er excitation but the competition from intrinsic carrier recombination is not yet very strong. Furthermore, the higher resistivity of GaN grown under slightly N-rich conditions is favorable for supporting high electric fields for hot carrier generation. GaN:Er is of special interest since it has been shown to be relatively immune to the thermal quenching seen in other Er-doped semiconductors and has the ability to incorporate significant concentration of RE ions without precipitation and without quenching the photoluminescence or electroluminescence intensity. These properties, in conjunction with the fact that GaN is a semiconductor and can provide charge carrier excitation of the Er ions (unlike insulators such as SiO:Er), meet the key requirements for an electrically pumped waveguide amplifier. GaN optical channel waveguides can be designed for use with the commercial material using the effective index method. GaN refractive index values of 2.35 and 2.25 at 632.8 nm and 1.5 μm. The fixed values of the width and film thickness could be calculated using the effective indices for the etched region and the unetched region. An etch depth of ~0.3 μm was chosen since the resulting structure would have an appropriate effective index difference and support only a few modes, limiting the effect of higher order lossy modes. An application area of GaN:RE technology is infrared optical telecommunications at 1.3 and 1.5 μm. The versatility and robust nature of RE-doped GaN technology holds great promise for optoelectronic and photonic applications (Steckl et al. 2002).

5.4.2 Erbium-Doped Semiconductor Waveguides

Erbium-doped semiconductor waveguide amplifiers (EDWAs) have been extensively explored due to their compact integrated size and the performance advantages inherited from Erbium-doped fiber amplifiers (EDFAs), namely low noise figure, negligible polarization dependence, good temperature stability and the absence of interchannel crosstalk to achieve performance comparable to EDFAs, a high doping level is required to compensate for the small optical transition cross-section of erbium (Er) as well as the waveguide length limit of a few centimeter to tens of centimeter, making essential the selection of Er-host materials which can avoid deleterious high concentration effects. There are many similarities in the fundamental basics of lasers and optical amplifiers, where the stimulated emission in both is achieved by maintaining a suitable degree of population inversion between an excited state and the ground state through either electrical or optical pumping. Thus, an Er-doped III–V oxide-based monolithically integrated waveguide optical amplifier can be readily modified for photon generation as either an incoherent amplified spontaneous emission (ASE) light source or an Er-doped waveguide laser (EDWL). An ASE source is basically an EDWA with no signal input, while an EDWL requires feedback through the incorporation of a resonant cavity achieved through high reflectance cleaved facets and/or deposited mirror coatings that are commonly used in III–V semiconductor diode lasers. With the growing field of fiber lasers and broadband ASE sources for sensing and other purposes, many applications might also benefit from this more compact, monolithically integrated planar waveguide implementation (Huang 2006).

Among rare earths, erbium belongs to the group of lanthanides, and is extensively studied due to the fortuitous coincidence of the near 1.55 μm optical transitions of Er with the minimum attenuation window of standard silica optical fibers. The optical properties of interest occur for trivalently ionized Er ions, Er^{3+}. These have the electronic configuration of Xe in common (1*s*22*s*22*p*63*s*23*p*63*d*104*s*24*p*64*d*105*s*25*p*6) with additional electrons added to the 6*s*-, 5*d*- and 4*f*-shells, respectively. The trivalently ionized Er ions have an electronic configuration of [Xe] 4*f*11, where the partially filled 4*f* shell is shielded by the outer 5*s*25*p*6 closed shells of the Xe configuration. Accordingly, the position of energy levels and related optical transitions are barely dependent on the surrounding host material into which the ions are incorporated. The different possible electronic configurations of 4*f* electrons introduce different energy states due to spin–spin and spin–orbit interactions. Erbium ions can be incorporated into a variety of host materials. In general, materials with ionic structures such as oxides, fluoride glasses or ionic crystals are better Er hosts than covalent semiconductors, offering a higher Er solubility in the solid phase for minimal clustering and segregation. Silica-based glass is the most widely used Er host due to its application in optical fibers. However, due to the small solubility of rare earth ions in silica (the suggested maximum Er concentration in silica for optimal amplifier performance is under 100 ppm), other glass materials have been developed such as

alumina, sodalime and phosphosilicate glass. Phosphate-based glasses are known to have a higher Er solubility, having been shown to accommodate several weight percent concentrations of rare earth oxides without clustering in rare earth-based bulk lasers. Aluminum oxides can be added to glass matrixes as network modifiers for both higher Er solubility and broadband emission. Rare earth concentrations of 2 % have been claimed without clustering in a host glass consisting 8.5 mol% of Al_2O_3. In addition to the solubility, the luminescence linewidth can be substantially affected by the host composition and the local environment where Er^{3+} ions locate. Besides the broadening by the Stark-splitting of energy levels induced by the local crystal field, the emission linewidth also contains the contributions from a homogeneous and inhomogeneous effect. For a transition between two energy states of an Er^{3+} ion, the homogeneous broadening arises from the lifetime of the states and depends on both radiative and nonradiative processes. The shorter the lifetime is, the broader the state. The inhomogeneous broadening are due to the multiplicity of sites and environments available to the Er ions. In glasses, both broadening can be quite large, as compared to crystal, and is very important for optical amplifiers. A broader emission linewidth covers more signal channels in dense wavelength division multiplexing (DWDM) systems, or provides a wider wavelength tuning range for EDWLs. Besides its effect as a network modifier, Al_2O_3 is known among various oxide glasses for its larger inhomogeneous broadening. The wet oxides of InAlP and AlGaAs usually contain a large amount of Al_2O_3 (and phosphate as in InAlP oxides), showing a broader emission linewidth and higher Er solubility. Most importantly, grown on GaAs, these host materials provide a unique feasibility for monolithic integration with active devices such as pump lasers, an advantage most glass materials don't have (Huang 2006).

In order to achieve very compact integration such as a long spiral of waveguide occupying a small area, a large core/cladding index contrast is needed to increase the optical confinement and reduce the bending loss. Semiconductor/oxide hybrid waveguide structures have been designed to combine the high refractive indices of semiconductors with a suitably positioned Er-doped oxide active layer. In this structure, the bottom cladding layer is a semiconductor layer with a lower refractive index, and the active Er-doped oxide layer is grown and implanted on top of a high refractive index semiconductor core layer. These two layers of oxide/semiconductor can be viewed as forming a composite waveguide core, where the active Er ions are placed along the top edge instead of near the center of the core. With most of the Er emission then guided through an underlying transparent semiconductor core through what is essentially a waveguide coupling mechanism (the emission from Er^{3+} ions can be stimulated via evanescence field and still be guided within the semiconductor core), this offset of the Er-active layer may also serve to reduce the undesirable excited state absorption (ESA). ESA occurs where an excited Er^{3+} ion absorbs a photon emitted at 1.53 μm from other Er^{3+} ions, boosting itself to a higher 4I9/2 energy level. To reduce scattering loss from the higher index contrast oxide/air interface, an optional top oxide cladding (SiO_2, Al_2O_3, SiN_x, etc.) can be deposited after Er-implantation. Due to the large refractive index contrast between the semiconductor and oxide layers, very strong optical confinement can be

achieved in very compact structures employing thinner waveguiding layers. In addition, the higher lateral index contrast of ridge waveguide structures enables smaller bend radius curved waveguides desirable for fabricating long spiral-coiled waveguides in monolithically integrated EDWA applications. Moreover, the epitaxially smooth interface possible between semiconductor layers may also help to further reduce the propagation loss compared to a fully oxidized heterostructure waveguide. As with semiconductor heterostructures, such composite semiconductor/oxide hybrid structures provide tremendous design flexibility through the variation of many parameters such as Al composition, and the order, number and thickness of layers. More advanced designs of this type will require simultaneous consideration of an optimization of waveguide optical mode confinement, the multilayer vertical reflectance properties and their influence on the VIP cavity, etc. As an example, in order to maintain a suitable waveguide structure while increasing the overall volume of the Er-doped InAlP native oxide active medium as required for high-power applications. An alternative design uses a multilayer structure containing buried Er-doped AlGaAs and InAlP oxides sandwiched between high-index, oxidation-resistant semiconductor layers (such as InGaP which has been used in MOSFET structures as an oxidation barrier layer), a composite core layer with a higher average effective index can be realized. To provide enough Er penetration in this core layer, Er-doping via multiple high-energy Er-implants is required, considering the thickness of the core and the heavy mass densities of both native oxides and un-oxidized semiconductors. Building on a GaAs platform, various schemes can be envisioned to monolithically integrate pump or signal lasers with Er-doped planar waveguides. Due to the high Er concentration required to reach a high gain per unit length, cooperative up-conversion interactions between the closely spaced Er ions can reduce the pumping efficiency such that a rather high pump power is required to obtain a net gain. The DBR mirror structure is realized by epitaxial growth of alternative quarter-wave optical thickness high (GaAs) and low (AlGaAs) index semiconductor layers. Appropriate P and N-type dopants are incorporated above and below the InGaAs quantum well active region to form the required P–N junction diode for electrical injection. An electroluminescent structure with only one bottom DBR mirror, sometimes referred to as a "half-VCSEL," is not itself a new concept, being utilized in early VCSEL devices having deposited top mirrors and, more recently, in high-power external cavity VCSEL devices. The reflectance of a top gold metal mirror need not match the high reflectance typically found in multilayer DBR reflectors because, with the use of Yb co-doping, even broad luminescence below lasing threshold can be effectively absorbed to pump the Er ions in the EDWA core. Lateral lasing in the quantum-well layer will naturally be prevented by use of spiral-coiled device geometry. Considering that the high-index Er-doped waveguiding structure does not extend down into the semiconductor active layer, the weak gain guiding will be insufficient to bend the light with low loss, and absorption in the un-pumped regions will attenuate light leaving the pumped regions. Further lateral losses in the QW layer can be introduced by use of diamond dicing saw cuts or etched Q-spoiling trenches where needed around the waveguide structure (Huang 2006).

5.5 Semiconductor Nanomaterials for Waveguides

Semiconductor nanowires have been developed to improve the stability of a wurtzite crystalline phase of standard III–V semiconductors such as InP and GaAs, which in their bulk forms always adopt a zincblende crystal structure. This dual stability results in the unanticipated challenge of producing single crystals during the growth process, as well as in necessitating characterization of these new forms of otherwise well-known semiconductors in terms of basic bulk material properties. While wurtzite–zincblende polytypism is known for III-nitride semiconductors, among the III-arsenides and III-phosphides it is unique to the nanoscale under ambient temperature and pressure conditions. For understanding exhibited linear and nonlinear optical properties, modeling the behavior of, or designing devices upon the nanostructures in which the wurtzite modification appears, the bulk material characterization is of both fundamental and applied interest. The uniaxial nature of wurtzite GaAs makes it naturally birefringent, distinguishing it from the normal cubic zincblende form of GaAs, which is spatially isotropic. Wurtzite crystals are consequently interesting as nonlinear media, since their birefringence makes phase-matching conditions possible to maximize nonlinear wave mixing processes, the simplest case of which is second harmonic generation (SHG). The exhibited SHG intensity has polarization dependences that originate from the form of the electrical susceptibility tensor. This is intimately related to the form of the Raman tensor, which of course is itself defined by a derivate of the susceptibility with respect to the atomic positions, as both are reliant upon the crystalline symmetry (Crankshaw 2009).

Semiconductor nanowires have attracted great interest both for basic studies of one-dimensional physics and as building blocks for nanoscale devices. Many III–V and II–VI material systems have been developed with various growth modes, such as laser-assisted catalytic growth and chemical beam epitaxy, as well as some catalyst-free methods such as selective-area epitaxy. The vapor–liquid–solid (VLS) growth mechanism is a common mode of synthesis, in which gas-phase reactants saturate a liquid metal catalyst and precipitate underneath to form a crystalline solid. When grown on [111]-oriented substrates, nanowires tend to align vertically, such that they are unclad, free-standing structures with a lateral dimension determined primarily by the size of the catalyst metal droplet. The multitude of parameters involved in any synthesis method has been optimized, including the VLS growth of InP nanowires. One striking feature observed in the nanowire growth is their ability to crystallize in the wurtzite structure, much like the GaAs nanoneedles. Although bulk InP always occurs in a zincblende crystal structure, both zincblende and wurtzite crystal phases have proven to be stable forms for nanowires made of InP and other typically zincblende III–V materials, indeed sometimes within the same nanowire structure. This presents the unexpected challenge of synthesizing nanowires with a uniform, single crystallinity, as well as the unexpected opportunity to investigate basic material properties of the new crystal forms. For example, a substantial blue-shift of the emission energy of

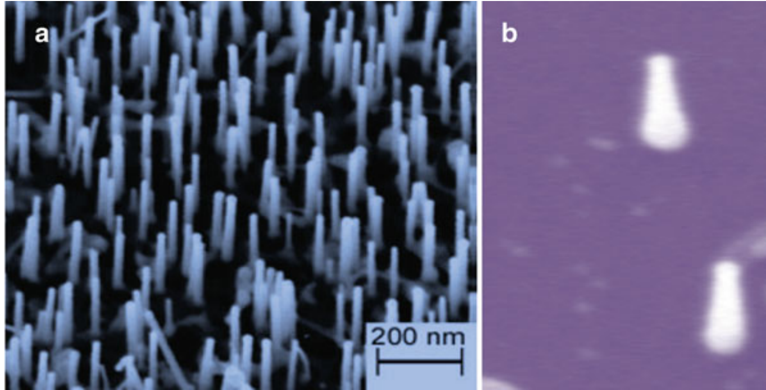

Fig. 5.9 InP nanowires (Crankshaw 2009): (**a**) quantum-confined, having an average diameter of ~16 nm; (**b**) the incorporation of an axial heterostructure within the nanowire (~300 nm in length, and ~20 nm in diameter)

wurtzite InP compared to zincblende InP have been investigated. As shown in Fig. 5.9a, InP nanowires are quantum-confined, having an average diameter of ~16 nm. InP nanowires were grown on (111) silicon substrates via the VLS growth mechanism in a MOCVD reactor. The incorporation of an axial heterostructure within the nanowire (NW)—an $InAs_xP_{1-x}$ section with InP barriers—which is rather unique in that the heterostructures in this material system are at NW diameters small enough to show quantum confinement. For this sample, the wires are ~300 nm in length, and ~20 nm in diameter, as shown in the scanning electron micrograph in Fig. 5.9b. With higher As fractions to push the wavelength into the 1.2–1.55 μm range, these structures could be useful for silicon photonics and optical telecommunications applications (Crankshaw 2009).

5.6 Summary

Semiconductor waveguides are generally made from elements of III–V, II–VI, or IV–VI, which have been mostly used for optoelectronic device applications, such as GaAs and InP. Compared to Si and Ge, GaAs and InP have high electron mobility and velocities, properties that are extremely important for the development of high speed electronic devices. Their direct band gaps and therefore their high radiative efficiency make them important for optoelectronic materials. An attractive feature of the binary compounds is that they can be combined or alloyed to form ternary or quaternary compounds, or mixed crystals. These compounds are made up of three or four group III and group V atoms and by choosing different binary compounds, it is possible to select different band gaps and therefore varying emission energies for light sources. A wide range of compound semiconductors can be exploited to access

a wide range of output wavelengths. However, by alloying it is possible to vary the band gap continuously and monotonically and together with it the band structure, electronic, and optical properties. The formation of ternary and quaternary compounds of varying band gaps also enables the formation of heterojunctions, which have become essential for the design of high performance electronic and optoelectronic devices.

Silicon waveguides have been primarily operated at wavelengths in the NIR, typically around 1.4–1.6 μm. This has been convenient due to the large number of commercial optical components available in this regime. The silicon is usually patterned with sub-micrometer precision, into microphotonic components. These operate in the infrared, most commonly at the 1.55 μm wavelength used by most fiber-optic telecommunication systems. The silicon typically lies on top of a layer of silica known as SOI. Moreover, porous silicon waveguides provide an interesting alternative to conventional SOI structures that could offer advantages for silicon interconnect waveguides, modulators and components. Porous silicon is a nanoscale composite material with an effective refractive index between that of air and silicon that can easily be fabricated in multilayer structures. GaAs/AlGaAs waveguides provide interesting optical properties for nonlinear optical signal processing. The optical Kerr coefficient of GaAs is approximately 4 times larger than that of crystalline silicon and three orders of magnitude larger than that of standard optical fiber. The key to realize on-chip integrated optical devices is working with a low-loss, highly nonlinear material system that allows the creation of both active and passive photonic devices. With quantum-well technology, III–V group semiconductors, such as GaAs and its alloys, can be used to create low-loss waveguides with very high second and third-order nonlinearities, or direct band gaps that enable the fabrication of bright lasing sources.

Many lanthanide elements have played an important role in various optoelectronic and photonic applications, ranging from emitting elements in solid-state lasers and in phosphors for color lamps and displays to optical waveguides. These rare earth (RE) elements have a partially filled inner ($4f$) shell shielded from its surroundings by completely filled outer ($5s$ and $5p$) orbitals. Due to this shielding, the intra $4f$ shell transitions result in very sharp optical emissions at wavelengths from the ultraviolet to the infrared (IR). In general, RE-doped conventional semiconductors (Si, GaAs, etc.) have exhibited limited photoemission at room temperature due low RE solubility and severe temperature quenching. The thermal quenching in Er-doped semiconductors decreases with increasing band gap. Therefore, WBGS are attractive hosts for RE elements.

Semiconductor nanowires have attracted great interest both for basic studies of one-dimensional physics and as building blocks for nanoscale devices. Many III–V and II–VI material systems have been developed with various growth modes, such as laser-assisted catalytic growth and chemical beam epitaxy, as well as some catalyst-free methods such as selective-area epitaxy.

References

Agrawal GP (1995) Nonlinear fiber optics, 2nd edn. Academic, San Diego
Apiratikul P (2009) Semiconductor waveguides for nonlinear optical signal processing. PhD dissertation, University of Maryland, College Park
Bristow AD et al (2007) Two-photon absorption and Kerr coefficients of silicon for 850–2,200 nmi (4,100 km). Appl Phys Lett 90(2):191104
Celler GK, Cristoloveanu S (2003) Frontiers of silicon-on-insulator. J Appl Phys 93(9):4955
Crankshaw SM (2009) Spectroscopic characterization of III-V semiconductor nanomaterials. PhD dissertation, University of California, Berkeley
Dekker R, Usechak N, Först M, Driessen A (2008) Ultrafast nonlinear all-optical processes in silicon-on-insulator waveguides. J Phys D 40:R249–R271
Deri RJ, Kapon E (1991) Low-loss III-V semiconductor optical waveguides. IEEE J Quantum Electron 27(3):626–640
Dimitropoulos D et al (2005) Lifetime of photogenerated carriers in silicon-on-insulator rib waveguides. Appl Phys Lett 86:071115
Ganguly P, Rahul S (2011) Silicon photonics: a solution for ultrahigh speed data transfer. ACEEE Int J Commun 2(3):26–31
GoldenMap (2013) Superlattice. http://en.goldenmap.com/Superlattice#. Accessed 25 Feb 2013
Hoogland S (2013) The fuss about quantum dots. http://www.photonics.com/Article.aspx?AID=31908. Accessed 23 Feb 2013
Huang M (2006) Erbium-doped wet oxides of AlGaAs and InAlP on GaAs substrates for optoelectronic integration. PhD dissertation, University of Notre Dame, Notre Dame
Jones R et al (2005) Net continuous wave optical gain in a low loss silicon-on-insulator waveguide by stimulated Raman scattering. Opt Express 13(2):519–525
Jussila H (2010) Fabrication of indium arsenide quantum dot structure for semiconductor optical amplifiers. Master thesis, AALTO University, Aalto-yliopisto Teknillinen Korkeakoulu, Espoo
Knights AP, Jessop PE (2007) Silicon waveguides for integrated optics. In: Calvo ML, Lakshminarayanan V (eds) Optical waveguides: from theory to applied technologies. CRC Press, Boca Raton, pp 231–270
Koos C et al (2007) Nonlinear silicon-on-insulator waveguides for all-optical signal processing. Opt Express 15(10):5976–5990
Narasimha A et al (2008) A 40-Gb/s QSFP optoelectronic transceiver in a 0.13 μm CMOS silicon-on-insulator technology. In: Proceedings of the optical fiber communication conference (OFC), OMK7
Nicolae CP et al (2006) Modulation instability in silicon photonic nanowires. Opt Lett 31 (24):3609
NRL (2013) Nonlinear optics in semiconductor waveguides. http://www.nrl.navy.mil/photonics/5654/nonlinearOpticsWaveguides.php. Accessed 26 Feb 2013
Shin J, Chang YC, Dagli N (2009) Propagation loss study of very compact GaAs/AlGaAs substrate removed waveguides. Opt Express 17(5):3390–3395
Sigal I (2010) Three wave mixing in periodically quantum-well-intermixed GaAs: AlGaAs superlattices: modeling, optimization, and parametric generation. Master thesis, University of Toronto, Toronto
Simatupang JW (2009) Vertical InGaAsP/InP taper FP-LD for injection-locking applications. Master thesis, National Taiwan University of Science and Technology, Taipei
Spott A et al (2010) Silicon waveguides and ring resonators at 5.5 μm. Appl Phys Lett 97:213501 (1–3)
Steckl AJ et al (2002) Rare-earth-doped GaN: growth, properties, and fabrication of electroluminescent devices. IEEE J Sel Top Quantum Electron 8(4):749–766
Stievater TH et al (2008) Low-loss suspended quantum well waveguides. Opt Express 16 (4):2621–2627

Vurgaftman I et al (2001) Band parameters for III-V compound semiconductors and their alloys. J Appl Phys 89(11):5815–5875
Younis U (2010) Monolithic integration for nonlinear optical frequency conversion in semiconductor waveguides. PhD dissertation, University of Glasgow, Scotland
Zhang J et al (2007) Optical solitons in a silicon waveguide. Opt Express 15(12):7682–7688